2018-07-25

Tailoring Isothermal Redox Properties of Calcium-based Perovskites

Yu, Ningyu

UNIVERSITY OF CALGARY

Tailoring Isothermal Redox Properties of Calcium-based Perovskites

by

Ningyu Yu

A THESIS

SUBMITTED TO THE FACULTY OF GRADUATE STUDIES

IN PARTIAL FULFILMENT OF THE REQUIREMENTS FOR THE

DEGREE OF MASTER OF SCIENCE

GRADUATE PROGRAM IN CHEMICAL ENGINEERING

CALGARY, ALBERTA

JULY, 2018

Abstract

Perovskite structured (ABO_3) redox materials are highly attractive for the advancement of a variety of sustainable processes such as Chemical Looping Combustion (CLC), thermochemical fuel production, etc. Apart from the state-of-the-art materials that require extreme synthesis and reaction conditions such as high temperature, simple perovskites that can operate at comparatively lower temperatures and are carbon resistant are strongly desired. This challenge was undertaken in the present thesis, and for this purpose, $CaMnO_3$ and its Fe substituted analogues were chosen. Isothermal redox properties of this material were investigated at various selected temperatures from 600°C to 900°C, demonstrating up to 15 cycles of consistent oxygen release/uptake capacity, with no noticeable amount of carbon deposition under any conditions used in the present study. Structural and compositional variations were monitored at different stages using SEM, EDS and wide angle XRD.

Acknowledgements

Primarily, I would like to thank Prof. Nader Mahinpey for giving me the opportunity of joining his group and provide me the facilities, advices and support to perform my research work within the framework of the Energy and Environment Research Group (EERG). I consider this as an invaluable opportunity that helped me to grow as a scientist. I would like to thank Dr. Mahesh Nair for his advices and suggestions to make my research work progress in a successful manner, and for spending a lot of time with me in the laboratory. His timely guidance and consistent support throughout my Master's tenure are greatly appreciated. I am also very much grateful to my examination committee members - Dr. Sathish Ponnurangam and Dr. Hector De la Hoz Siegler - for their important comments and advices that shaped my thesis in a stronger way. Finally, I extend my sincere gratitude to all the members of the Energy and Environmental Research Group, especially Dr. Davood Karami, Mr. Pradeep Shrestha and Ms. Camilla Fernandes De Oliveira, for their insights and suggestions during my research work and thesis writing.

I gratefully acknowledge the funding support received from the NSERC-IRC Program, Canadian Natural Resources Limited, Devon Canada Corporation. Last but not least, thanks to all my friends and family members who were, and are, supportive during my difficult times; their help and companionship made my time in Calgary very joyful and unforgettable.

Dedication

This thesis is dedicated to my parents and my beloved fiancée. Their unconditional encouragement, trust and support taught me to embrace both personal and professional challenges.

Table of Contents

List of Tables

List of Figures and Illustrations

List of Symbols, Abbreviations, Nomenclature

Abbreviation	Definition
CLC	Chemical Looping Combustion
CLOU	Chemical Looping with Oxygen Uncoupling
EDS	Energy Dispersive Spectroscopy
GSAS	General Structure Analysis System
IPCC	Intergovernmental Panel on Climate Change
OC	Oxygen Carrier
SEM	Scanning Electron Microscopy
TGA	Thermogravimetry Analysis
XRD	X-ray Diffraction

Symbol	Definition
r_A	Empirical radii of A-site cation in perovskite structure
r_B	Empirical radii of b-site cation in perovskite structure
r_O	Empirical radii of oxygen in perovskite structure
R_o	Oxygen carrying capacity
R_p	Profile R-factor
R_{wp}	Weighted-profile R-factor
t	Goldschmidt tolerance factor
T	Temperature
Δm_{ox}	Mass gain during oxidation in TGA
Δm_{red}	Mass loss during reduction in TGA
χ^2	Goodness factor

CHAPTER 1: INTRODUCTION

1.1 Background

Developing clean and efficient energy technologies has been a theme being explored for decades. In recent years, redox cycling of metal oxides has attracted considerable attention of the scientific community due to their applications in various fields such as solar thermochemically splitting of H_2O or CO_2 [1-3] solid oxide fuel cells [4, 5] air -separation [6, 7] and Chemical Looping Combustion (CLC) of hydrocarbon fuels [8-10].

1.1.1 Chemical-looping Combustion

The rising amounts of CO_2 in the atmosphere in conjugation with the diminishing amounts of fossil derived fuels puts forward the need for developing alternate energy technologies. Even though tremendous progress has been achieved with regard to solar cells and fuel cells, the concerns regarding atmospheric CO_2 levels still persists. The report of the Intergovernmental Panel on Climate Change (IPCC) indicates that the average CO_2 concentration has been raised 30% from around 300 ppm to the high-level milestone of 400 ppm in 2013 [11]. This increase in anthropogenic CO_2 concentration is believed to be leading to the warming of the earth's due to the well-known famous greenhouse effect [12]. Therefore, an inclusive solution to the two-fold energy crisis lies in the effective utilization of CO_2. For this purpose, a variety of CO_2 capture and conversion technologies are being investigated globally.

For CO_2 capture, there are several approaches available such as pre-combustion, post-combustion separation, and oxy-fuel combustion [13]. Intensive energy input is necessary

for these strategies, which would result in decreasing energy efficiency significantly. On the other hand, Chemical Looping Combustion (CLC) technology was proposed to avoid such energy penalties, capturing CO_2 in a more efficient manner [14]. In general, CLC involves metal oxides (oxygen carriers) circulating between two interconnected fluidized bed reactors: one acting as a fuel reactor utilizing lattice oxygen from metal oxide for fuel oxidation and the second one being an air reactor, where oxygen carriers could be re-oxidized by contacting with air. The concept is illustrated in Figure 1.1 and the overall reactions stoichiometry with hydrocarbon fuels in the two reactors are shown in equation 1.1 and 1.2 respectively [15].

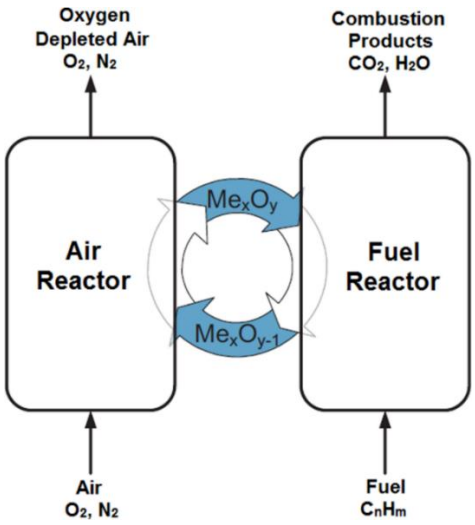

Figure 1. 1 Principle of chemical looping combustion (Me_xO_y represents oxidized metal oxide, Me_xO_{y-1} represents reduced metal oxide)

Fuel reactor: $(2n + m)M_yO_x + C_nH_{2m} \rightarrow (2n + m)M_yO_{x-1} + mH_2O + nCO_2$ (1.1)

Air reactor: $M_yO_{x-1} + \frac{1}{2}O_2 \rightarrow M_yO_x$ (1.2)

Thus, CO_2 can be obtained from the flue gas of the fuel reactor. Further separating H_2O from the mixture would result in concentrated CO_2. On the other hand, exhaust gas stream of the

air reactor, which mainly contains N_2 and remaining O_2 can be discharged into the ambient without causing contamination problems. In the meantime, the reduced metal oxides are transported between these two reactors, and redox reactions are taking place in a cyclic manner [16]. Briefly, the development of highly efficient metal oxide oxygen carriers (OC) which are stable and carbon resistant are to be achieved for the further advancement of this technology.

1.1.2 Other Applications

A step further, a variety of recently developed CO_2 conversion techniques also primarily require highly efficient oxygen carrier materials. For example, solar thermochemical CO_2/H_2O splitting utilizes the oxygen exchange properties of metal oxides. This idea provides a feasible method for generating the industrially important syngas CO and H_2. Utilizing the entire spectrum of solar radiation is a very attractive advantage for this solar driven technology, as opposed to solar electricity technique, where only specific spectrum regions could be used for generating electricity. Consequently, the production of H_2 or CO via solar heat has the potential of being far more efficient than photoelectrical H_2 or CO production. In this case, the major difference between this technique and CLC is that CO_2/H_2O is used as the oxidant other than air. A classic example of the oxygen carrier applied in this concept is CeO_2 with fluorite structure. The material CeO_2 can be partially reduced to $CeO_{2-\delta}$ thermally at high temperature (~1400 °C) [17-20]. The efforts to improve the material performance will be discussed in the section below. Redox properties of metal oxides also find applications in air separation and solid oxide fuel cells (SOFC).

1.2 Oxygen Carrier Development History

Development of materials with satisfying redox properties is essential to successfully operate the related redox applications. The desired properties for a suitable oxygen carrier candidate to be applied to redox processes such as CLC are given as follows:

- Desired thermodynamic and kinetic properties
- High stability during multiple redox cycles
- Resistance against attrition and high mechanical strength.
- Environmental friendly and low costs.

Various types of oxygen carriers have been investigated. Especially for chemical-looping combustion, researchers have studied around a thousand of oxygen carrier combinations, among which the majority of the materials were synthesized with binary/tertiary active metal oxides supported on various types of inert binders [21-53]. Development history of oxygen carriers is reviewed in order to give the main achievements reached during last decades in developing this technology.

1.2.1 Binary Metal Oxide

Numerous binary transition metal oxides have been investigated by researchers as potential oxygen carriers. Ni-based materials has been studied extensively as oxygen carriers for CLC application in the literature. At elevated temperature (900℃-1100℃) CLC condition, Ni-based oxygen carriers presented satisfying performance of high reaction rate for redox reactions [21]. However, researchers have observed decreasing performance of such material

along multiple redox cycles due to carbon deposition problem. Moreover, CO and H_2 production were detected since Ni catalyzes methane splitting simultaneously as a side reaction [22]. Also, toxicity of Ni element makes the material less environmentally friendly, additional safety measures are always recommended to take into place. To overcome problems such as strong agglomeration tendency of Ni-based oxygen carrier, inert materials are utilized to act as the support. As one of the most popular support, alumina was reported to hinder agglomeration of the active phase significantly during the redox cycles. However, formation of $NiAl_2O_4$ was detected as Ni/NiO could react with the alumina support in the experimental conditions. $NiAl_2O_4$ is a stable mixed metal oxide, which is not easy to be reduced with temperatures less than 1000°C [21]. To compensate the issue of losing Ni-based materials into $NiAl_2O_4$ during the redox cycles, alumina support can be modified through thermal or chemical treatment or using $NiAl_2O_4$ directly instead [13, 23]. YSZ (Yttria-Stabilized Zyrconia) is also considered to a possible support material, as it was reported to increase the oxidation rate of NiO. However, major drawback of YSZ is its high cost for industrial application at the current stage [24]. Other inert support candidates including SiO_2 and ZrO_2 have been investigated as well [23, 24]. The reactivity of these supported materials was observed to decrease gradually after repeated redox cycles due to formation of nickel complexes phases.

Unlike Ni, Cu-based materials possess large oxygen storage capacity and have high reaction rate with no thermodynamic restrictions. Furthermore, applying CuO as oxygen carrier has a unique advantage, where both redox reactions are exothermic, which would make the CLC process more energy efficient. These favorable properties make Cu-based oxygen carriers excellent candidates for converting hydrocarbon fuel to CO_2 and H_2O completely in an

efficient manner without carbon deposition problem [25]. In addition, lower cost and environmentally friendly behaviors make the materials more attractive. However, the major problem with Cu- based materials are their low melting point and poor mechanical strength, which results into strong tendency to agglomeration during the redox cycles under CLC conditions [26-28]. The mechanical strength of the Cu-based materials is dependent on the metal loading and support applied. For SiO_2 supported Cu-based materials, reactions between support and active metal oxide was not observed at chemical looping of methane in a fixed bed reactor reveal that after 20 cycles at 800°C [29].

Fe-based materials are attractive for their abundant available resource and being nontoxic, despite of lower oxygen transport capacity and CH_4 conversion compared to other materials [22, 30, 31]. The materials also show low tendency of carbon deposition on the surface [32]. Various forms of iron oxides including hematite (Fe_2O_3), magnetite (Fe_3O_4) and wustite (FeO) exist due to the different oxidation state of Fe [33]. Only transformation between hematite and magnetite is preferred for CLC purpose [25]. The reason is that further reduction of iron oxide to Fe would result into partial oxidation production formation such as CO and H_2. Similarly, general inert supports to increase mechanical strength and specific surface area are Al_2O_3, $MgAl_2O_3$, SiO_2 and TiO_2 [13, 24, 34-35]. However, Corbella *et al*. reported that the oxygen transporting capacity of Fe_2O_3/TiO_2 is diminishing, because of $FeTiO_3$ formation between the active metal phase and its support [35].

Mn-based materials are another group of oxygen carrier candidate for its availability and non-toxicity. The materials show higher oxygen transport capacities compared to iron

counterparts [36]. Similar to iron-based materials, there exist various oxidation states for manganese during the redox reactions as well. MnO_2 is not stable with temperature higher than 500°C, while Mn_2O_3 and Mn_3O_4 is more thermodynamically stable under CLC operating temperatures within air atmosphere [37]. As a result, the oxygen is released and incorporated between the form of Mn_3O_4 and MnO during CLC operations [38]. To tackle the problem of low reactivity for bulk Mn-based materials, efforts have been taken to select proper supporting materials to improve the performance. Satisfying results have not been found with common supports such as Al_2O_3, SiO_2 and TiO_2 for Mn-based carriers [27, 39-41]. ZrO_2 has shown good reactivity as the supporting material for Mn-based carrier under repeated redox cycle. However, the combination was observed to have tendency to agglomerate [22, 42]. Compared to CLC of methane combustion, the material is more favorable in splitting methane into CO and H_2 [43].

Researchers also investigated the possibility of cobalt-based materials, expecting to achieve desirable performance as oxygen carriers. In redox reactions, Co could exist in several different oxidation states. Since CoO is more stable compered to Co_3O_4 at higher temperature range (> 900 °C), cycling transformation between CoO and Co is taking place at CLC conditions [44]. When supported with materials such as Al_2O_3 or TiO_2, interaction between the active phase of Co-based oxygen carrier and the supports were reported, forming unreactive compounds. As a result, the application of Co-based materials under CLC redox conditions is limited, due to its poor regenerability, low conversion and slow reaction rate [26].

CeO_2 has drawn interests in solar thermochemically splitting of CO_2/H_2O. The material started to draw people's attention when Chueh *et al.* [45] first successfully demonstrated that ceria-based material undergone a nonstoichiometric redox behavior ($CeO_2 \leftrightarrow CeO_{2-\delta}$) in a solar reactor for ten successive cycles in 2010. The production syngas ratio (H_2:CO) can be adjusted by changing oxidant ratio (H_2O: CO_2). Even though the transferable oxygen capacity of ceria is less than its iron-based counterparts, sintering problem is not serious due to its high melting point [46]. As a result, adopting support material to stabilize the active phase is not considered to be necessary. In addition, oxygen diffusion rate is very fast because of the oxygen transport pathway formed due to the structural defect [47, 48]. The thermodynamic and kinetic properties of ceria can be further tailored by doping with transition metals and rare earth metal oxides.

1.2.2 Mixed Binary Metal Oxides

Single binary metal oxides including oxides of Ni, Cu, Fe, Mn, Co and Ce were extensively investigated. In most cases, these metal oxides have to be supported by inert substrate materials to overcome problems such as weak mechanical strength, low structural stability, low reaction kinetics in order to enhance their reaction performance. However, interactions between inert support and metal oxide phases under CLC conditions were reported for some combinations. The formation of undesired stable phases would result into decreasing the efficiency of oxygen carrier performance. Consequently, besides the efforts in improving binary metal oxide system mentioned above, the idea of applying mixed binary metal oxides was proposed as another effective approach to enhance the redox properties of oxygen carriers such as conversion, mechanical strength, reactivity and stability. The following paragraphs present some examples of mixed metal oxides, which have been studied.

Sajen *et al.* [49] synthesized a new type of oxygen carrier ($CuMn_2O_4$) by mixing Cu and Mn oxides. It was also observed that the synthesized combination could be regenerated at 800°C with presence of air. The material presented satisfying mechanical strength and stable performance in a packed bed reactor. Hossain and coworkers [50] investigated the performance of a Co promoted alumina-supported Ni oxygen carrier CLC application for a fluidized bed CLC process. The existence of Co successfully reduced the formation of $NiAl_2O_4$ between Ni and the Al_2O_3 support interaction. The oxygen carrier oxygen capacity was increased by minimizing side reaction of active phase Ni, which promoted more Ni involved with redox reactions. Jin *et al.* [51] further studied the CoO-NiO system supported on YSZ. Slight reaction kinetics was observed compared to individual metal oxides due to the formation of impure phases $NiCoO_2$. However, the Co-Ni/YSZ oxygen carrier show high extent of regenerability and excellent performance in avoiding the issues of carbon deposition. Son *et al.* [52] tested Fe-Ni/bentonite in a CFB with various Fe-Ni/bentonite ratios and proposed an optimum ratio of 3 (NiO/Fe_2O_3=75:25). Siriwardane *et al.* [53] optimized CuO and Fe_2O_3 composition ratios to enhance the performance of the oxygen carrier materials. Their research indicated synergetic effect between CuO and Fe_2O_3 improved the performance of pure CuO in terms of material stability.

1.2.3 Perovskite Oxide

Perovskite are ternary oxides represented by formula ABO_3. The cation sites are occupied generally by a larger A^{m+} and a smaller B^{n+} ion [54]. The structure can be represented with smaller B cation residing at the center, forming an octahedron with surrounding oxygen ions around which A cations are arranged as in the corners, forming a cube. Alternatively, the

perovskite can be treated as a cubic unit cell built from corner-sharing BO_6 octahedra, with A cation in the centre [55]. Both the possible representations of perovskite structure are schematically depicted in Figure 1.2.

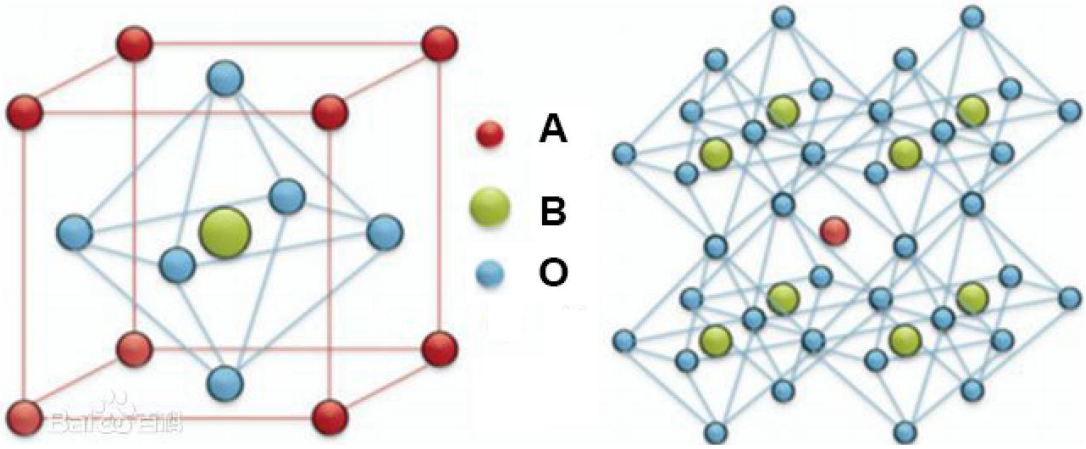

Figure 1. 2 Two different representations of the ideal perovskite structure

In general, the ideal cubic structure are rare and common distortions such as orthorhombic and rhombohedral can be found [56, 57]. The tolerance factor could be adopted to measure the deviation from the cubic structure as shown in Equation 1.3. The t-value is unity for an ideal cubic structure. The perovskite structure is also found to be maintained with Goldschmidt tolerance factor (t values) between $0.75 < t \leq 1$, with some distortions as mentioned above.

$$t = \frac{r_A + r_O}{\sqrt{2}(r_B + r_O)} \tag{1.3}$$

where r_A, r_B and r_O are empirical ionic radius for A-, B- and O-site ions respectively. In addition to the requirements imposed by the tolerance factor, electroneutrality is another important aspect that needs to be taken into consideration for a perovskite structure. As a

rule, the sum of cationic charges must be balanced by the anionic charge. This results in distribution of the charges such as $A^{l+}B^{5+}O_3$, $A^{2+}B^{4+}O_3$ and $A^{3+}B^{3+}O_3$. However, the cationic or oxygen anionic non-stoichiometry is frequently encountered in this type of materials resulting into the formation of defective lattice structure [55]. For example, $LaMnO_{3+\lambda}$ has shown non-stoichiometry of oxygen excess, which resulted from vacancies at the A- and B-site proven by neutron diffraction studies, while $LaNiO_{2.5}$ possesses oxygen deficiency forming anionic vacancies [58, 59]. The unique property of perovskite to possess defective structures make this category of materials excellent candidates for redox applications. The unique perovskite properties can be attributed to the versatility of the compositions of perovskite structural materials. Large number of metallic elements could be selected to fit into the perovskite structure as illustrated in Figure 1.3.

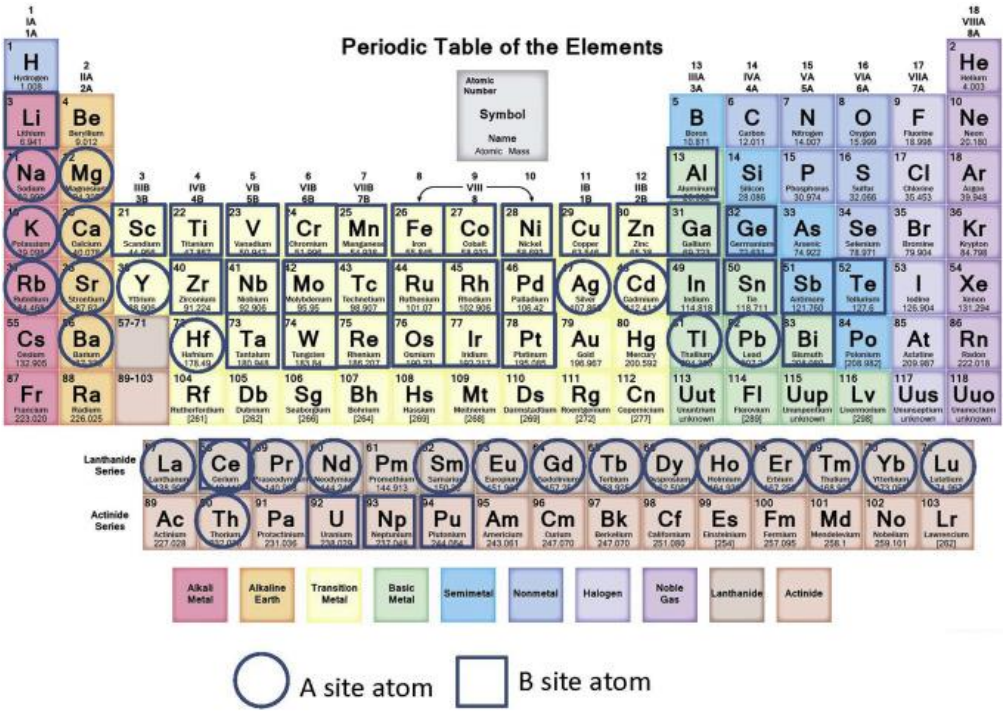

Figure 1. 3 Chemical elements that can be involved in perovskite structure oxides [60]

The physicochemical properties of these materials can be widely tailored by accommodating A/B-site cations in the structure, either partially or completely. In addition, the rich redox chemistry inherent in perovskite oxides makes them appropriate to be used as oxygen carriers for a variety of sustainable energy applications. The following paragraphs give a brief review on the efforts invested into perovskite development.

Sarshar *et al*. [61] investigated performance of various members of the $La_{1-x}Ce_xBO_3$ (B=Co, Mn) series under multiple oxidative and reductive cycles in a fluidized reactor. It was observed that the materials possessed higher stability with lower CH_4 pressure. When increasing the pressure of CH_4, partially oxidized products were detected as the product of side reactions. Rydén *et al.* [62] observed that $La_{0.5}Sr_{0.5}Fe_{0.5}Co_{0.5}O_3$ could effectively catalyzing oxidization of CH_4 into H_2O and CO_2 at 900°C. Increasing Sr concentration could enhance the oxygen availability of the perovskite but lower its reactivity with methane. The authors suggested that the loss in performance of the perovskites during repeated redox cycles is due to agglomeration of the particle. Another perovskite with the composition of $CaMn_{0.875}Ti_{0.125}O_3$ was studied by Leion *et al.* [63] for Chemical Looping with Oxygen Uncoupling (CLOU). The performance with excellent conversion of methane together with high chemical stability continuous CLC systems were observed. These results have demonstrated the promising potential of perovskite-based systems and encourage more comprehensive and extensive research efforts to be put in discovering perovskite-type materials.

In conclusion, various transition metals oxides and their mixture combinations have been studied by scientists for CLC purposes. Generally, these metal oxides are supported on an

inert support providing high surface areas as well as enhancing the mechanical strength, fluidizability, and attrition resistance. Two major concerns in this case are high temperature sintering and carbon deposition problem. The objective of this thesis is to develop a suitable perovskite structured oxygen carrier material for CLC and study its corresponding redox behavior.

1.3 Syntheses Strategies

Tremendous efforts were made in the past to develop a synthetic route for preparing perovskite structured oxides with optimized textural properties. The selection of a specific route depends on the expected application of perovskites since it would bring variations in the morphology and properties of the product. Regarding heterogeneous catalysis, specific surface area is playing an important role. As a result, the synthesis methods were focused on obtaining crystalline materials with high specific surface area in most of the cases. Similarly, for redox applications specific surface area is essential along with the ability of release and uptake oxygen in a sequential manner. A well defined porous structure is favourable on this regard to overcome mass transfer and diffusion limitations. Generally, traditional synthetic methods of perovskites can be divided into the solid-state routes and wet chemical routes. Several typical advanced methods enabling high specific surface areas will also be introduced in the following paragraphs.

1.3.1 Solid-state Methods

Solid-state ceramic method, developed in 1970's, is the oldest method for synthesizing perovskite structured mixed metal. It involves mixing metal precursors homogeneously. High temperature (>1500°C) calcinations for long durations (24h) are necessary to promote the

crystallization of the desired perovskite phase, forming agglomerated grains and limited specific surface area, generally less than 5 m^2g^{-1} [64-66].

Later, microwave method was introduced as another solid-state method by Rao *et al.* [67] to replace prolonged thermal treatment for the ceramic route. In this synthesizing route, precursors are calcined by microwave irradiation of 2.45 GHz for a few minutes (less than 10 minutes) to transform into perovskite without long thermal treatment process. These authors reported the successful syntheses of $LaCrO_3$, $LaCoO_3$ and $LaNiO_3$ crystalline perovskites with nanometer sizes by this method from precursors such as oxides or nitrates. However, the specific surface areas resulted from this preparation method were not mentioned or discussed in their reports.

1.3.2 Liquid Phase Methods

Motivated by higher specific surface area preferred for predominantly majority of catalytic reactions, various low temperature (~800°C) wet chemical synthesis strategies were developed to obtain materials with enhanced surface area. Selected methods in this category will be thoroughly discussed in the following paragraphs.

Co-precipitation is a method for preparing relatively homogeneous perovskite powders using precursors such as hydroxides carbonates or nitrates without particle agglomeration. In this method, soluble precursors containing desired metal cations are mixed with precipitation agent under supersaturation conditions. After a series of operations such as filtration, washing, and drying, the obtained amorphous precipitate powder will transform into crystalline perovskite after calcination at relative lower temperature (800°C). During the co-

precipitation reactions, parameters such as solution concentration, temperature, pH are important, because they are major factors to affect the morphology and particle size distribution of the products. [68-70] Perovskites prepared by co-precipitation method are found to be homogeneous and possessing satisfying purities, while the specific surface area was not enhanced significantly to around 10 m^2/g [71].

Numerous sol-gel techniques are developed to be other alternative approaches for perovskite synthesis with enhanced surface area. Among these Pechini method is regarded as a popular one for its versatility in synthesizing perovskites [66, 70]. The basis of the synthesis route is built on completely mixing highly soluble salts with desired cations, then added into a solution of citric acid and ethylene glycol. The resulted citrate complexes are believed to balance the individual behaviour of interested metallic ions in solution, which help form a more homogeneous ion distribution and hinder the separation of components in the future treatment steps. Later, the solution will be transferred into a polymer gel under controlled heating stages. Removal of the polymer matrix will result in highly homogeneous precursor, calcination of which results in crystalline and phase pure perovskites. Citric acid is used as the complexing agent in most cases. However, other compounds such as lactic, tartaric, maleic or oleic acids can also function as complexing agents [72]. In this case, it was reported that by maintaining the porosity to some extent, the specific surface area of the final product could reach up to 25 m^2g^{-1}. The significant advantages of such method are highly crystallized perovskite structures with little amount of impurities in the final product [73].

The freeze-drying (FD) and spray-drying (SD) are other synthesizing routes to fabricate perovskites. The idea of the freeze-drying method is to rapidly cool the fine solution droplets

in which the precursors were dissolved to preserve the initial homogeneity of the ion mixing solution. The frozen solution is then transferred to a shell freezer under vacuum where the solvent will sublimate. Then, the obtained low-density and porous solid will be calcined to from well crystallized perovskite. In spray-drying, the solvent is evaporated after spraying on the heated surface by controlled sized spray nozzle. The size of the final perovskite product can be tailored by controlling the concentration of precursor solutions and droplet sizes. Highly homogeneous perovskite oxides with controllable morphology and composition properties can be achieved by both methods [70, 74, 75].

1.3.3 Other Advanced Methods

In 2000, Kaliaguine *et al.* developed a synthesis method called reactive grinding method which could increase the specific surface area of produced nanocrystalline perovskite oxides to more than 100 m^2g^{-1} [76]. The main idea and one of the greatest advantages of this method is replacing thermal energy for perovskite crystallization by mechanical energy provided by the ball-mill reactor at low temperature (≈40ºC). In this method, agglomeration and sintering issues of the particles during the high-temperature thermal treatment can be avoided, thus enhancing the specific surface area of the perovskite products significantly. The synthesized perovskite after this post-treatment with additive has specific surface areas above 80 m^2/g after calcination at 200°C [70, 78, 79].

More recently, templating methods were developed to synthesize porous perovskites with controlled pore structure and high specific surface area (up to 150 m^2g^{-1}) [80-82]. The concept of this method is similar to the traditional casting procedure, where an organic molecule (in the case of soft templating) or an inert solid oxide (in the case of nanocasting)

is used as structure directing agents. However, nanocasting is taking place in nanometer length scale. Typically, the precursors will be initially impregnated inside the template with certain structure. Then converting the precursors to the desired product and followed by the removal of the template by the leaching process using HF or NaOH solutions. The parent materials inside the pore structure are transferred into the product with its pore structure as replica of the template walls. Silica such as KIT-6, SBA-15 and SBA-16 are the most popular hard templates to make high-specific surface area perovskites for the diversity in their 3D ordered mesoporous structure and particle morphology [83]. An advantage of the hard template nanocasting method is the tunable pore size and pore structure by using suitable templates and processing conditions. Applying this method, Wang *et al.* [84] synthesized $LaCoO_3$ perovskite with ordered mesoporous structure, possessing a large surface area of around 100 m^2/g and a three-dimensional ordered mesostructured by using vinyl silica as hard template. In another study, Nair *et al.* [85] synthesized $LaMnO_3$ perovskites using SBA-15 as the hard template. High specific surface areas of 190 m^2/g were measured for these perovskites. The perovskite products with enhanced specific surface area are also proved to be high efficient methanol oxidation catalysts. Even though, several milestones were achieved in all these cases so far, the high temperature structural stability remain poor in these materials and efforts are still required to develop such materials with enhanced stability for high temperature applications (> 500°C).

Another advanced perovskite oxide synthesis option is hydrothermal method, which is carried out in autoclaves at elevated pressure. One advantages of this method is its low synthesizing temperature (less than 300 °C), which replaced the high calcination temperature as in the ceramic solid-state reaction route [86, 87]. Perovskite synthesis performed by many

researchers have demonstrated the viability of this approach. The morphology can be tuned significantly by changing the processing condition. In the same year, Zhang *et al.* [88] successfully fabricated phase pure $La_{0.5}Ca_{0.5}MnO_3$ nanowires under hydrothermal conditions at 275°C for 30 h. An interesting study regarding the hydrothermal synthesis of perovskites was performed by Chai *et al.* [89] in 2007. They synthesized $La_{0.5}Ba_{0.5}MnO_3$ perovskites various morphologies by adjusting the alkalinity of the reaction solution. Their study showed that the flower-like structures was formed via a nucleation-aggregation-crystallization growing process, while the cube like structures grew following a nucleation-crystallization path due to the variations in the reacting solution alkalinity. In addition, lower alkalinity was observed to increase the particle size in the cubic structures. Even though lots of perovskite with multiple morphologies have been fabricated, this method still needs efforts to apprehend the factors for synthesizing perovskites [90]. The summarize of various synthesizing strategies mentioned in the previous paragraphs is presented in Table 1.1.

Table 1. 1 Synthesis method of perovskite structured mixed metal oxides

Synthesis Method	**Purity**	**Calcination temperature**	**S_{BET} (m^2/g)**
Ceramic solid-state	Poor	>1000°C	<5
Microwave	Excellent	600-800°C	Not mentioned
Co-precipitation	High	800°C	10
Sol-gel	Excellent	800-1000°C	20
Spray drying/Freeze	Excellent	700-1000°C	Not mentioned
Reactive grinding	Moderate	550°C	10-105
Nanocasting	High	500-700 °C	100-150
Hydrothermal	High	No calcination step	Not mentioned

1.4 Problem Statement and Research Motivation

The development of novel metal oxide oxygen carriers remains the bottle neck for the advancement of a variety of sustainable processes. Even though several milestones were achieved using transition metal based binary oxides, issues including structural stability and carbon deposition are yet to be solved. Perovskite structured (ABO_3) mixed metal oxides with a rich redox chemistry and physicochemical properties are proven to be ideal on this regard and have recently been applied to a variety of redox processes such as Chemical Looping Combustion (CLC), thermochemical fuel production, etc. In these materials, the oxygen non-stoichiometry (δ), can be varied by changing parameters such as temperature and pressure. However, most promising perovskites developed so far constitutes multiple cationic substitutions that require extreme synthesis conditions such as high temperature. Therefore, design and activity monitoring of simple materials that can operate at comparatively lower temperatures and are carbon resistant are highly desired and challenging. For this purpose, the research interests of this thesis focus on studying isothermal redox properties of the perovskite oxide material $CaMnO_3$ at various selected temperatures (600°C – 900°C) under CLC operating conditions. In addition, since fundamental insights are rather scarce, regarding the effect of B-site substitution on the redox performance of this interesting material, studies were carried out by incorporating cationic substitution in this thesis. Varying amounts of Fe substitution were carried out in the B-site of $CaMnO_3$.

1.5 Objectives

The overall research goal of this thesis is to synthesis and to study the composition and structure behaviors of $CaMnO_3$ under isothermal redox conditions and the effect of Fe

substitution on the redox properties of $CaMnO_3$. Therefore, the research work is divided into the following specific objectives:

1. Synthesis a series of perovskite oxides including pristine and Fe substituted $CaMnO_3$ using Pechini method.
2. Investigation of the important physicochemical properties with comprehensive characterization techniques in the following aspects:
    a. Phase compositions (XRD)
    b. Structure morphologies (SEM)
    c. Surface elemental distribution (EDS)
3. Analysis of the reactivity of the prepared perovskite oxide materials in a Thermogravimetric analyzer (TGA) under the isothermal CLC of methane conditions.
4. Analysis of the stability and structural integrity of the materials in multiple redox cycles.
5. Investigation of the phase change behaviors with a gaseous CLC fuel such as methane.

1.6 Organization of the Thesis

Chapter one gives an overall introduction to the background of redox materials applications and development history as well as the structure and synthesis strategies of the perovskite oxide materials. Based on all the discussions, the motivation for this study is delivered and the objectives are stated. Chapter 2 explains the characterization techniques used to describe the perovskite oxides and the experimental synthesizing methods. Chapter 3 presents the studies on the redox properties of undoped $CaMnO_3$. Its structural and compositional behaviors were comprehensively probed at different temperatures with various characterization techniques and thermogravimetric analyzer. Chapter 4 further examined the

effect of B-site substitution with Fe on $CaMnO_3$. The redox activity and stability were tested. The performance was correlated with tolerance factor, electronegativity and surface element configurations. The conclusions and suggestions for future work are given in Chapter 5.

CHAPTER 2: EXPERIMENTAL SECTION

2.1 Synthesis of Perovskites

The corresponding chemical amounts of $CaMnO_3$ and a series of Fe substituted perovskite materials are listed in Table 2.1. They were synthesized by Pechini method using metal nitrates as precursors. The Pechini method has the advantage to achieve improved chemical homogeneity on the molecular scale with lower calcination temperature compared to traditional ceramic method.

Table 2. 1 Synthesized Perovskite formulation in this thesis

Sample ID	$Ca(NO_3)_2 \cdot 4H_2O$	$Mn(NO_3)_2 \cdot 4H_2O$	$Fe(NO_3)_3 \cdot 9H_2O$	Citric Acid	Ethylene Glycol
CMO	1.181 g	1.255 g	-	2.882	0.621 g
CFM5P	1.181 g	1.192 g	0.101 g	2.882	0.621 g
CFM19	1.181 g	1.130 g	0.202 g	2.882	0.621 g
CFM28	1.181 g	1.004 g	0.404 g	2.882	0.621 g
CFM37	1.181 g	0.879 g	0.606 g	2.882	0.621 g
CFM46	1.181 g	0.753 g	0.808 g	2.882	0.621 g
CFM55	1.181 g	0.628 g	1.01 g	2.882	0.621 g

Stoichiometric amounts of desired cation metal nitrates $Ca(NO_3)_2 \cdot 4H_2O$, $Fe(NO_3)_3 \cdot 9H_2O$, and $Mn(NO_3)_2 \cdot 4H_2O$ (all ≥ 97% purity, Sigma-Aldrich) and citric acid $C_6H_8O_7$ (≥ 99% purity, Sigma-Aldrich) were dissolved in 30 ml deionized water. The amount of citric acid was adjusted to attain a ratio of 1.5 with total metal ions. After complete dissolution, ethylene glycol (citric acid: ethylene glycol = 1.5:1) was added and kept stirring for 3 h more. This solution was transferred to an oven preheated to 80°C and dried for 48 h. The resultant dry foamy mass was ground well and calcined at 900°C for 5 h in a programmable muffle furnace

using the temperature−time profile presented in Figure 2.1, producing finely powdered dark gray samples.

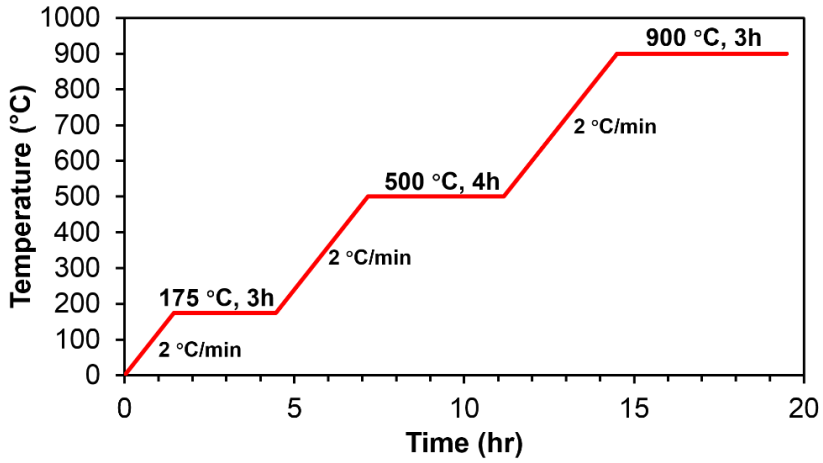

Figure 2. 1 Temperature program for calcination

The sample synthesis of $CaMnO_3$ procedure via the Pechini method is shown in Figure.2.2.

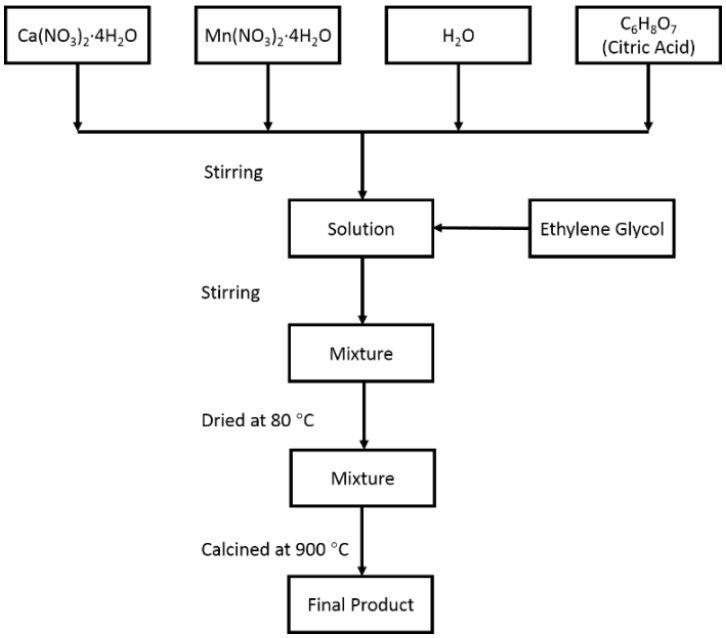

Figure 2. 2 Sample synthesis procedure via Pechini method

The numbers in the formulas represent the molar percentage of each element on B site of the perovskite oxides (For example, CMO is the short form of $CaMnO_3$, CFM37 is the short form of $CaFe_{0.3}Mn_{0.7}O_3$, and CFM5P is the short form of $CaFe_{0.5}Mn_{0.95}O_3$)

2.2 Characterization Methods

Comprehensive characterizations are necessary to be performed to reveal the properties of the synthesized materials such as crystallinity, phase identities, textural morphologies and surface properties. XRD, SEM and EDS were used to thoroughly understand the prepared perovskite oxide materials and are summarized in the following paragraphs.

2.2.1 Powder X-Ray Diffraction (XRD)

The XRD analysis is a reliable non-destructive technique to identify crystalline phases or determine material structure properties. Materials can be recycled after conducting XRD analysis. During a typical XRD measurement, electrons are accelerated by high voltage in the X-ray tube and collide with a metal anode target. X-rays are produced when outer orbital electrons occupy the vacant left by ionized electrons of the k shell. Since the transition energy solely depends on the nature of the element, every element has its characteristic spectrum. The most commonly used anode material is copper. When an X-ray beam strikes the crystalline powder, the selective scattered beam diffraction will be captured by an X-ray detector and recorded as a function of angle only if the glancing angle satisfies the Bragg law. The intensity of diffractogram at certain angle depends on the constructive and destructive interference among X-ray diffracted. The relationship between the scattering angle and the distance of lattice planes is given by Bragg´s law:

$$n\lambda = 2d \cdot \sin\theta \quad (2.1)$$

where n is the order of diffraction, λ is the wave length of incident X-ray, d is the distance between the reflecting planes and θ is the angle between the incident beam and the scattering plane. Bragg's law demonstrates the relationship between interplanar distance *d*, and the reflection angle θ as illustrated in Figure 2.3.

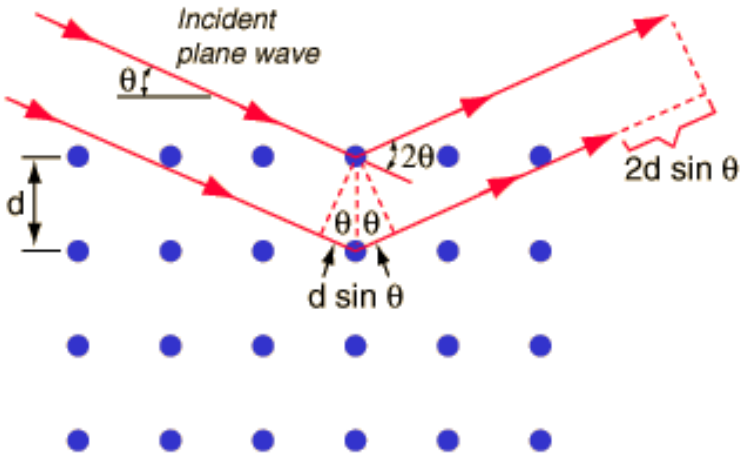

Figure 2. 3 X-rays being reflected by crystallographic planes [91]

Each individual crystalline compound has its unique powder x-ray diffractometer pattern, characterized by angle of reflection and intensity of each reflection. Comparison of the position and intensity of the reflections with those of known materials leads to a qualitative phase identification.

In this thesis, all XRD patterns were obtained from a Rigaku Multiflex X-ray Diffractometer with Cu Kα radiation (λ =0.15418 Å) as the X-ray source. The full diffractogram for each

analyzed material were recorded in the 2θ range of 20° to 80° scanning speed of 2.0°/min, at 40 kV tube voltage and 44 mA tube current. Identification of crystalline phases was performed by comparison with standard diffraction patterns (powder diffraction file PDF-2, International Center for Diffraction Data, ICDD) in MDI Jade 7.

Rietveld method, which was developed in 1960s by Hugo Rietveld, was used to further study crystal structures of the perovskite oxide materials synthesized in this thesis. Rietveld refinement analysis is developed to estimate the intensities of diffraction peaks in an XRD pattern to retrieve structural information about crystalline materials. During the refinement process, least square methods are carried out to obtain the best fit by minimizing of the residual S, which is the difference between an experimental XRD profile and calculated pattern. The formula for calculating S is given in Equation 2.2:

$$S = \sum_i w_i (y_{io} - y_{ic})^2 \quad (2.2)$$

where $w_i=1/y_{io}$, y_{io} is the observed intensity at step i and y_{ic} is the calculated intensity at step i. When performing the refinement, parameters such as crystal structure (unit cell, atom positions and displacement parameters, etc.), instrumental and specimen parameters (scale factors, peak broadening, the background, preferred orientation, etc.) could be varied to improve the match between observed and calculated diffraction patterns. To achieve better refinement result, a good structure model is necessary to initiate the process.

The goodness of fitting between the observations and the model is estimated by R-factors. These R-factors are error factors that are minimized as the fitted pattern approaches the

experimental pattern. Smaller R-factors represent better fitting approaches. The R-values used in this thesis are the profile R_p and the weighted profile R_{wp}. The R-factors are given in Equation 2.3 and 2.4. In this thesis, Rietveld refinement is mainly performed using GSAS (General Structure Analysis System) software package to study the cell parameter changes upon substituting Fe cation on B-site of $CaMnO_3$ perovskite crystalline structure.

$$R_p = \sum|y_{io} - y_{ic}|/(\sum y_{io}) \tag{2.3}$$

$$R_{wp} = [\sum w_i(y_{io} - y_{ic})^2/(\sum w_i y_{io}^2)]^2 \tag{2.4}$$

Another quality factor used is the chi square (χ^2), also known as goodness factor, given in Equation 2.5.

$$\chi 2 = \sum w_i(y_{io} - y_{ic})^2/(N - P) \tag{2.5}$$

where N is the total number of independent observations in all histograms and P is the number of refined parameters. It is generally accepted that a good refinement is achieved with R factors less than 10% and χ^2 less than 2.

2.2.2 Scanning Electron Microscopy (SEM) & Electron dispersive X-ray spectrometry (EDS)

SEM is an essential technique to characterize the solid surface morphologies through high-resolution imaging. During this characterization, the sample is interacted with a focused electron beam as a source of illumination. The electrons are generated by a schottky field

emission gun and are accelerated through a column towards the sample in the sample chamber. The electron beam is condensed by a condenser and focused by an objective lens. As a result, signals consisting of mainly secondary electrons (SE), high-energy backscattered electrons (BSE) and X-rays will be emitted. The SEM images are generated based on signals with varying intensity coming from the sample. Specifically, the low-energy secondary electrons give the information about topography of the sample. On the other hand, the backscattered electrons are closely dependent on the atomic weights of elements presented in the specimen. Thus, it can be used to differentiate surface elements of the sample based on the atomic weight. The working principle of SEM is demonstrated schematically in Figure 2.4.

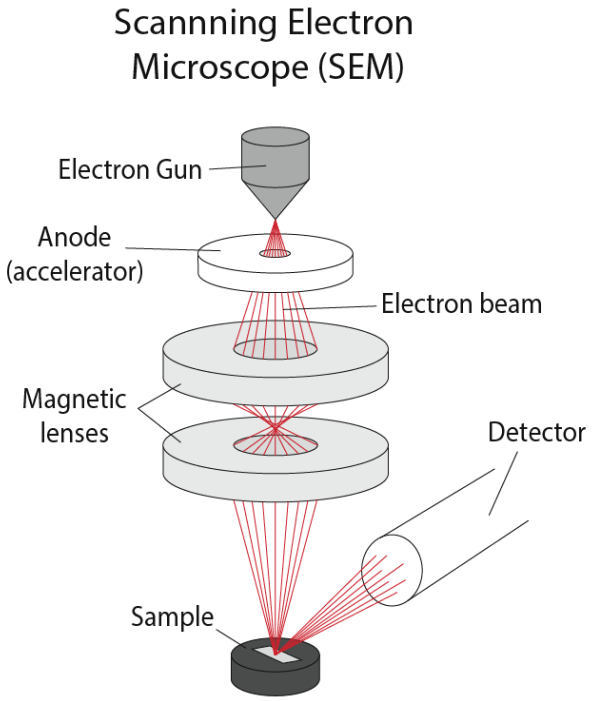

Figure 2. 4 Schematic diagram of SEM [92]

Electron dispersive X-ray spectrometry (EDS) is an additional analytical technique usually attached to the SEM equipment and used for elemental composition analysis of the sample. It is based on the emitted X-ray signal generated when high energy electron falls into the low energy level to fill the vacancy. The emitted X-ray is uniquely dependent on the element species. Consequently, the X-ray can be utilized to qualitatively analyze the elemental content of a selected area in specimen. In this work, the prepared perovskites were analyzed using this technique to determine the distribution of interested elements.

In this thesis, the SEM images of the studied materials were obtained at magnification ranges of 5,000X to 200,000X with an electron beam of 15 kV, using a FEI Quanta 250 FEG field emission scanning electron microscope. EDS (energy dispersive spectroscopy) analyses of the samples is performed with a Quantax 5030 Silicon Drift Detector.

2.3 Redox Activity Monitoring Experiments

Thermogravimetry is a technique for measuring mass change of a substance under varying gas atmospheres and temperatures. Isothermal redox behavior including oxygen capacity and thermal stability of the prepared perovskite materials were evaluated in a thermogravimetric analyzer (NETZSCH TG 209 F1 Libra). In a typical run, approximate 20 mg of oxygen carrier were placed into an alumina crucible. The thermal balance was calibrated with an empty alumina crucible under before each experiment. The reduction step was performed under an CH_4 flow (99.999% purity, <2 ppm O_2) with varying concentration from 10% to 30% at appropriate temperatures (600-900°C) for 7 minutes. Re-oxidation of the partially reduced oxides was performed under air (50%, balanced with Nitrogen) at the same corresponding temperature for 15 minutes. Between each reduction and re-oxidation step,

there is a 6-minute inert gas (N_2) purge to avoid mixing of combustible reducing agent with air. All heating and cooling steps were performed with a ramp rate of 45 °C/min. Both reduction and re-oxidation flow rates are 20 ml/min at ambient pressure. In this thesis, materials were tested for 1 redox cycle for initial redox behavior evaluation and for 15 cycles for further stability investigation. The programmed redox cycles are designed to mimic CLC operating condition to study the redox properties and behaviors of the perovskite oxide materials. The oxygen release during reduction induced a mass loss (Δm_{red}), whereas oxygen incorporation during re-oxidation induced a mass increase (Δm_{ox}). The mass variations were used to determine the oxygen carrying capacity (R_O) of the carriers and defined as follows:

$$R_O = \frac{(m_{ox} - m_{red})}{m_{ox}} \qquad (2.7)$$

Where Δm_{red} represents the oxygen release during reduction induced a mass loss, whereas Δm_{ox} stands for oxygen incorporation during re-oxidation induced a mass increase.

CHAPTER 3: ISOTHERMAL REDOX PROPERTIES OF $CaMnO_3$

3.1 Abstract

Perovskite structured mixed metal oxides (ABO_3) are one promising category of redox materials widely investigated for applications in various sustainable processes. In this study, we monitored the compositional and surface structural evolution of $CaMnO_3$ under redox conditions at selected temperatures. The redox efficiency and stability of $CaMnO_3$ was found to be temperature dependent. Despite enhanced sintering resistance and phase stability at 600°C, the amount of oxygen release/uptake was low. At 750°C, phase changes were found to diminish the redox efficiency in the long run. In contrast, at higher temperatures (900°C) stable oxygen uptake/release capacity was observed despite significant extent of sintering and the associated structural and phase changes. The present study indicates that material composition and temperature determine the redox chemistry of $CaMnO_3$ perovskite oxides. Interestingly, no noticeable amount of surface carbon deposition was detected under any stages of operation for this material.

3.2 Introduction

Perovskite oxides (ABO_3) constitute one of the most widely studied category of materials for applications in various sustainable processes including heterogeneous catalysis, redox reactions and electrochemistry [93-96]. Physicochemical properties of these materials can be tailored in accordance with the desired applications by varying the A/B/O-site compositions. Partial or complete incorporation of active metal cations in the lattice and redox stability by accommodating anion non-stoichiometry, are considered to be the most important attributes of perovskites. Materials that can release/uptake oxygen in a cyclic manner are highly desired for the advancement of emerging sustainable energy applications including solar

thermochemical fuel production, chemical looping combustion (CLC) and solid oxide fuel cells [97-99]. Significant efforts were recently made to modify the redox efficiency of perovskite structured oxygen carriers by integrating enhanced oxygen non-stoichiometry while maintaining structural stability [78, 100-102]. Unfortunately, noteworthy performance among perovskites is achieved mostly in the case of complex multi-component substitutions in the cationic sites and at high temperatures, mostly exceeding 1000°C, stimulating major stability concerns.

On the other hand, $CaMnO_3$ is recently emerging as a promising candidate owing to its comparatively low temperature redox chemistry (<1000°C). Performance evaluation along with kinetic and thermodynamic investigations were recently carried out for this material in CLC and air separation where high oxygen mobility, tolerance for multiple cation substitutions and high temperature stability were observed [103-105]. Even though with all these interesting traits, studies to tailor the redox properties of $CaMnO_3$ are still focused on multiple cation substitutions in the A and/or B-sites. However, variations in compositions leading to cation segregation during redox cycling could deteriorate the efficiency [106]. Hence, efforts are inevitable to obtain the insights regarding the evolution of composition and microstructure as a function of temperature to further optimize the redox chemistry of $CaMnO_3$.

3.3 Experimental Section

Polycrystalline $CaMnO_3$ perovskite oxide was synthesized by following the Pechini method. Stoichiometric amounts of metal nitrates, citric acid and ethylene glycol were used as the

precursors. In a typical synthesis, $Ca(NO_3)_3 \cdot 6H_2O$, $Mn(NO_3)_2 \cdot 4H_2O$ and citric acid were dissolved in 30 ml distilled water. The molar ratio between Ca and Mn was fixed to be unity. The amount of citric acid was adjusted to attain a ratio of 1.5 with total metal ions. After complete dissolution, ethylene glycol (citric acid: ethylene glycol = 3:2) was added and kept stirring for 3 h more. This solution was transferred to an oven preheated to 80 °C and dried. The resultant dry foamy mass was ground well and calcined at 900 °C for 5 h, to obtain phase pure $CaMnO_3$.

X-ray diffraction (XRD) was performed on a Rigaku Multiflex X-ray diffractometer with a Cu Kα radiation (λ = 0.15418 nm, 2θ = 20 - 80, steps = 0.02 2θ, recording time = 2s). Identification of crystalline phases was performed by comparison with standard diffraction patterns (powder diffraction file PDF-2, International Center for Diffraction Data, ICDD). XRD was used for phase identification of the fresh and materials recovered after use. The particle morphology and surface structure were analyzed using a high-resolution field emission scanning electron microscope (FEI Quanta 250 FEG), with an electron beam of 15 kV. EDS Analyses were performed with Quanta 5030 Silicon Drift detector. Monitoring of the surface structure evolution during the redox cycling of $CaMnO_3$ was performed at selected temperatures (600, 750 and 900 °C). The heating stage was performed with a ramp rate of 30 °C.min^{-1} under N_2 atmosphere, followed by reduction step with pure CH_4 and re-oxidation step with pure O_2 respectively while keeping the low vacuum pressure of 100 Pa. High voltage of 25 kV was used throughout the high temperature SEM operation.

Isothermal redox experiments were performed using a Netzsch TG 209 F1 TGA. The balance was calibrated with an empty alumina crucible. Sample masses of approximately 20 mg were used for each analysis. Thermal reduction step was performed under CH_4 (10-30% in N_2) for 7 minutes and re-oxidation was performed under O_2 (10% in N_2) for 15 minutes. Isothermal redox steps were performed at selected temperatures (600, 750 and 900 °C). All heating and cooling steps were programmed with a ramp rate of 45 °C.min^{-1}.

3.4 Results and Discussion

In the present study, we synthesized phase pure and crystalline $CaMnO_3$ perovskites by following the Pechini method (see experimental section). This method is facile and well-studied, and the perovskites thus obtained were previously found to exhibit better redox chemistry and stability [102]. CH_4 was used as the reducing agent and O_2 was used for re-oxidation, as in CLC. Variations in the composition, non-stoichiometry and microstructure during the reduction and re-oxidation, were examined. Monitoring of surface structure evolution was performed using high temperature scanning electron microscopy (SEM). In this case, images were collected under isothermal conditions during CH_4 induced reduction and re-oxidation under O_2, at selected temperatures between 600 – 900°C. The wide-angle powder X-ray diffraction pattern obtained at room temperature confirmed the presence of $CaMnO_3$ after calcination at 900°C. At lower temperatures, reflections corresponding to impurity phases were also observed (Figure 3.1).

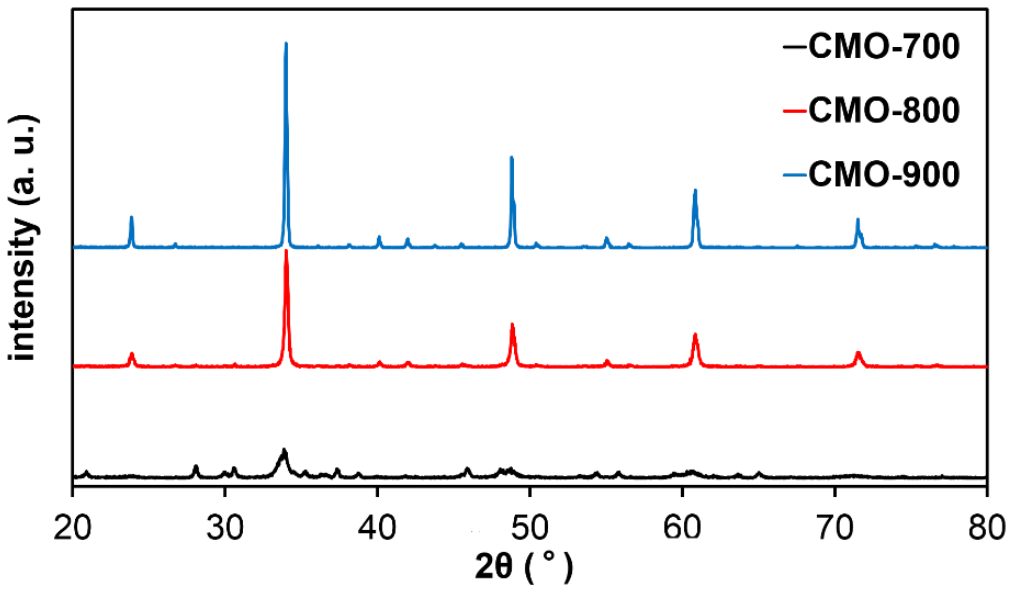

Figure 3. 1 Wide angle XRD patterns of $CaMnO_3$ calcined at 700, 800 and 900°C

Reflections corresponding to any binary oxide impurities were not observed in the wide-angle region indicating the absence of phase segregation for the material calcined at 900°C (CMO-900). Later on, room temperature SEM analysis was performed to obtain information regarding morphology and surface structure, and representative images are provided in Figure 3.2. Randomly agglomerated dense particles with irregular morphologies were observed for CMO-900. Different from other perovskite compositions synthesized by similar methods, inter-particle pores were clearly visible to a large extent. From high magnification SEM images, it is clear that the material consists of primary particles of approximately 150 nm, which were strongly agglomerated to form further large crystallites. Elemental mappings were performed on this material and the results indicate rather uniform distribution of the cationic species along with oxygen, throughout the surface of $CaMnO_3$. Such presence of

surface oxygen in a uniform manner is the core to facilitate the redox activity in oxygen carriers.

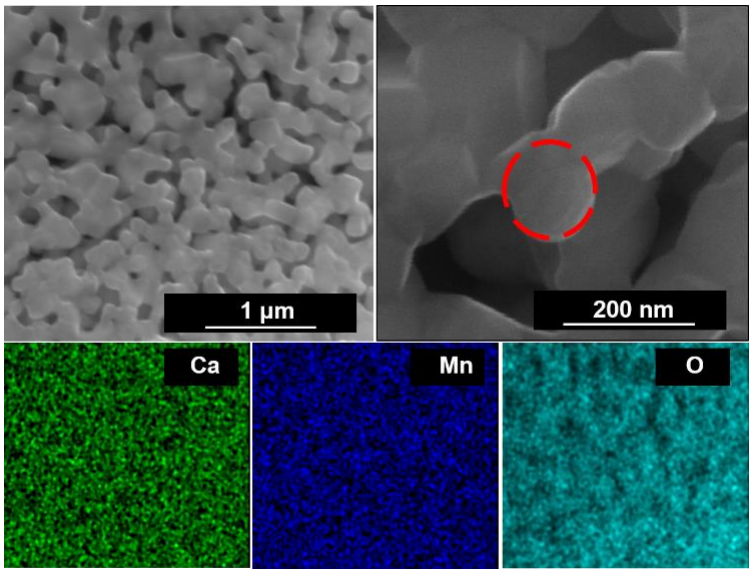

Figure 3. 2 SEM images of as-synthesized $CaMnO_3$ calcined at 900°C. Elemental mappings for the corresponding regions are shown for Ca, Mn and O.

Thermochemical redox schemes in CLC over perovskites generally constitute CH_4 induced reduction and re-oxidation under O_2 (~1000°C) [107]. On the other hand, solar processes for splitting CO_2 and H_2O utilizes concentrated solar energy for carrying out thermal reduction (~1400°C) followed by re-oxidation producing CO and H_2 respectively. Here also, recent attempts were reported to bring down the reduction temperature by coupling with partial oxidation of CH_4 [108]. However, success in carrying out these redox reactions under isothermal conditions at lower temperatures are limited. Our studies clearly indicate noteworthy isothermal redox activity for as synthesized $CaMnO_3$ between 600 – 900°C (Figure 3.3). Redox performance of perovskite oxides at temperatures as low as 600 °C, is rarely observed and in this study, a reduction extent of $\delta = 0.14$ was observed for $CaMnO_3$

during the CH_4 induced reduction step. During the simultaneous isothermal re-oxidation under O_2, a δ value of 0.14 was obtained indicating total re-oxidation.

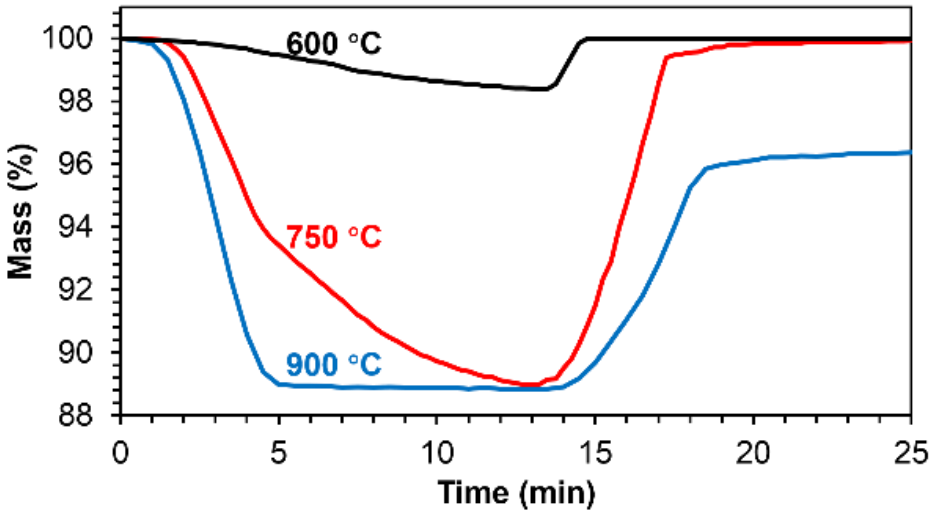

Figure 3. 3 Isothermal reduction and re-oxidation profiles of $CaMnO_3$ at selected temperatures

Wide angle XRD analysis was performed for materials recovered after reduction and re-oxidation at this temperature. Interestingly, the observed patterns in either case demonstrate that the perovskite structure remained intact during the complete cycle (Figure 3.4 and Figure 3.5).

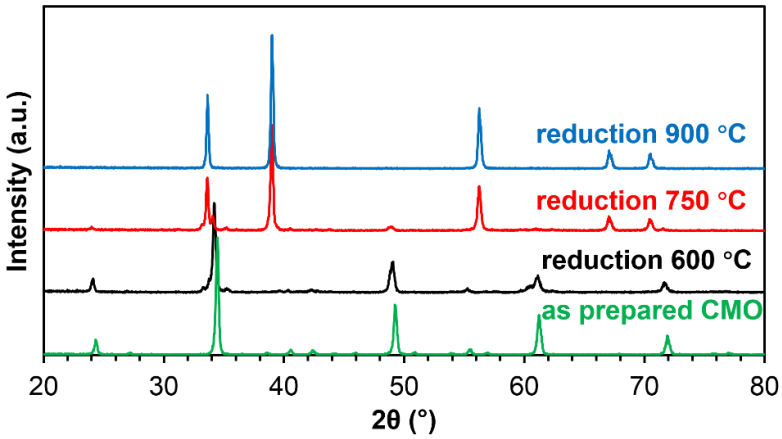

Figure 3. 4 Wide angle XRD patterns of $CaMnO_3$ perovskites recovered after reduction at 600, 750 and 900°C.

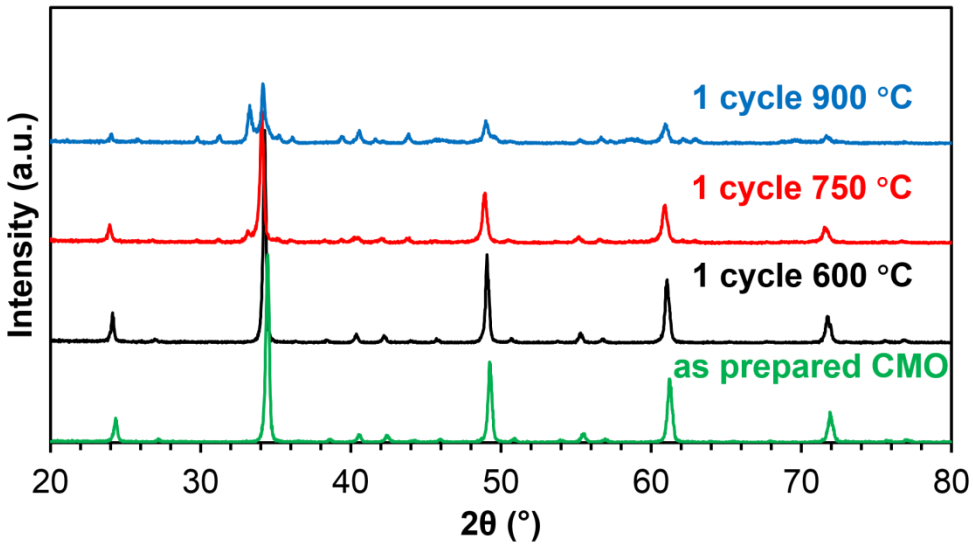

Figure 3. 5 Wide angle XRD patterns of $CaMnO_3$ perovskites recovered after re-oxidation at 600, 750 and 900°C.

Further, at 750°C, an enhanced extent of reduction was observed. Here again, the oxygen uptake during the re-oxidation was found to regain the initial perovskite structure after one complete cycle. Wide angle XRD patterns after reduction indicates the destruction of perovskite structure leading to the formation of $Ca_{0.5}Mn_{0.5}O$. Perovskite structure was regained during re-oxidation in this case, however, with the presence of some minor impurity

peaks. One probable reason is that even though surface oxygen is replaced back during the re-oxidation step, complete incorporation of the lattice oxygen back into the structure is hindered. The reduction extent at 900°C is the same as that obtained at 750°C. Total re-oxidation is seldom achieved in this case. Initial reduction destroyed perovskite structure forming $Ca_{0.5}Mn_{0.5}O$ which on re-oxidation resulted in the formation of $CaMnO_{2.5}$. Presence of some $CaMnO_3$ cannot be excluded in this case since some peaks in the wide angle XRD of the recovered material after one cycle can also be indexed to $CaMnO_3$. These results clearly indicate that even though the reduction process remains the same, temperature predominantly determines the nature of the material during re-oxidation in the first cycle.

Later, redox experiments were conducted by varying CH_4 partial pressure and the obtained profiles are shown in Figure 3.6. At 600°C, the evolution of δ values after the reduction step was found to vary according to the partial pressure of methane. However, at 750°C and 900°C, the δ values remained consistent irrespective of the partial pressure variations performed in the present study. This could be because of the fact that theoretical maximum was already achieved. Considering all these results, it can be concluded that temperature predominantly determines the redox chemistry of this material, during the first cycle.

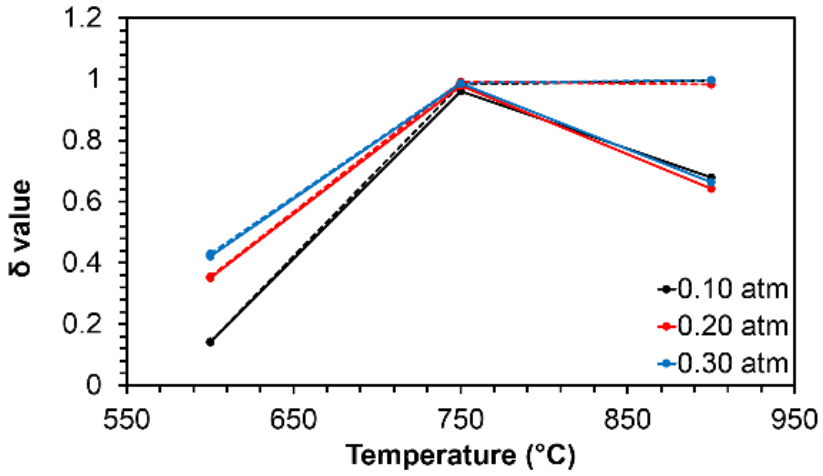

Figure 3. 6 Evolution of δ values as a function of temperature at various partial pressures of CH_4. Dashed lines correspond to reduction and solid lines corresponds to re-oxidation

To obtain information regarding the redox stability at 600°C, long term experiments were conducted for 15 cycles and obtained redox profiles are shown in Figure 3.7. Even though lower, constant reduction and re-oxidation extents were observed during the entire period and perovskite structure was found to be retained after 15 redox cycles as evident from the wide angle XRD patterns given in Figure 3.8. However, at 750°C, strong deactivation was observed for this material after two cycles. No reflection corresponding to the perovskite structure was observed for the material recovered after 15 cycles at 750°C.

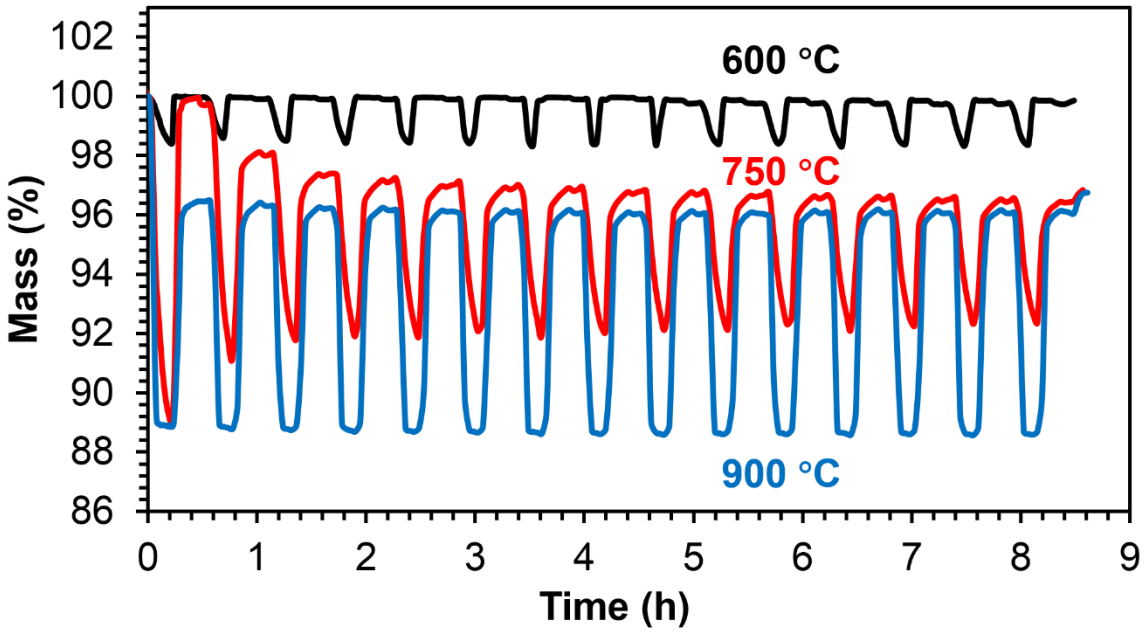

Figure 3. 7 Isothermal reduction and re-oxidation profiles of $CaMnO_3$ at 600, 750 and 900°C for 15 cycles.

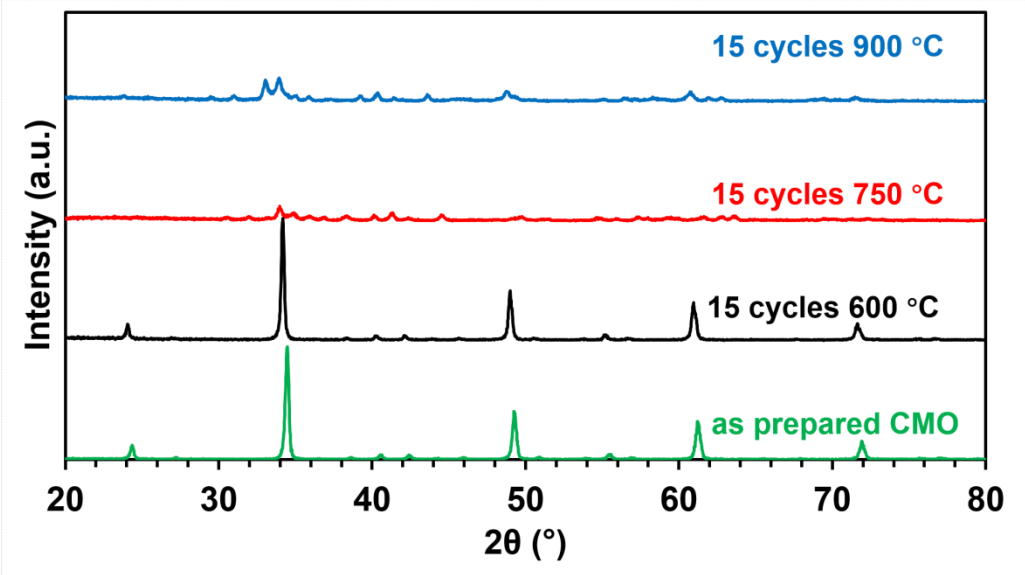

Figure 3. 8 Wide angle XRD patterns of $CaMnO_3$ perovskites recovered 15 redox cycles at 600, 750 and 900°C

The observed pattern was entirely different from the one obtained for the material recovered after one cycle shown in Figure 3.4. It is clear that the variations in phase progresses along with the number of cycles at 750°C. On the other hand, excellent redox stability was exhibited by $CaMnO_3$ at 900°C for 15 cycles. In this case the material recovered after stability tests belonged to $CaMnO_{2.5}$. This clearly indicate that in contrast to what observed at 750°C, variations in material composition take place only during the first cycle at 900°C and the resulting $CaMnO_{2.5}$ exhibited highly stable redox performance throughout the period of study. One further interesting observation is that irrespective of the temperature and duration of the reaction, $CaMnO_3$ totally resisted CH_4 splitting reaction and thereby the carbon deposition, for up to 30% of CH_4 in the reactant feed. Consequently, no indication of carbon deposition over the redox material was observed at any temperatures which can be confirmed by the absence of a mass variation profile corresponding to carbon deposition between the reduction and re-oxidation steps.

As mentioned before, further performance enhancement of the $CaMnO_3$ for redox cycling and for other high temperature applications, may be achieved by utilizing these materials with well-defined morphologies and/or pore structures. Advanced approaches to overcome the stability concerns can possibly be developed from the insights obtained by monitoring the high temperature structural evolutions during the redox cycles. Such information may also be used to derive the mechanistic aspects of redox processes. In combination, these can critically contribute towards the modification of the existing processes and to design novel material combinations for applications in sustainable redox processes. Such efforts are scarce in the literature [109] and therefore high temperature SEM studies were performed to monitor the variations in surface structure in $CaMnO_3$ during redox process (Figure 3.9). These results

clearly indicate excellent microstructural stability during reduction and re-oxidation at 600 and 750°C. This means significant variations in the specific surface area or porosity were not observed.

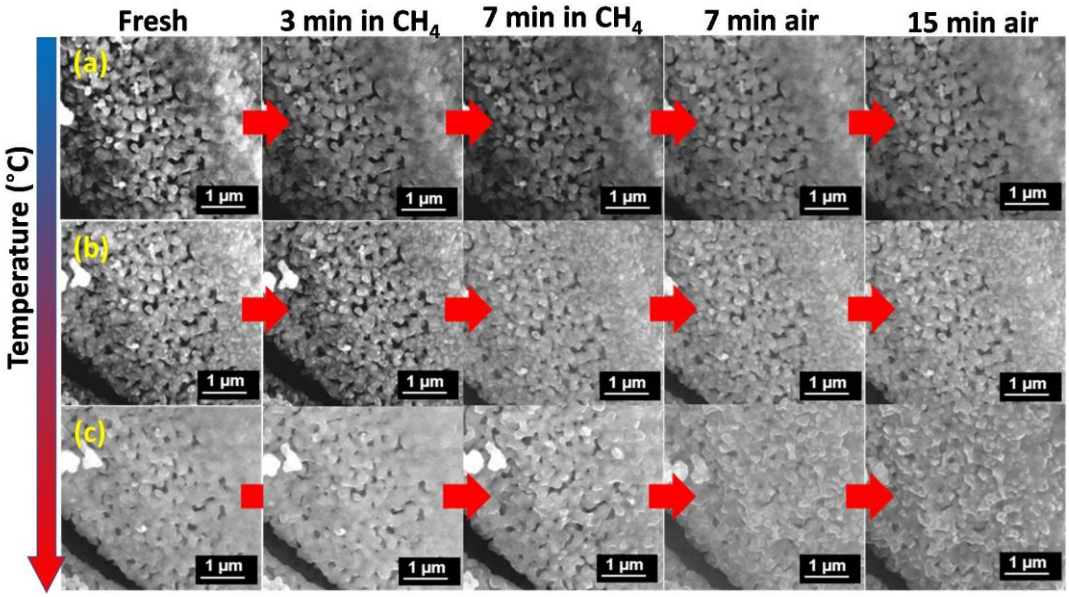

Figure 3. 9 In situ SEM images of $CaMnO_3$ obtained during reduction/re-oxidation cycles at 600°C (a), 750°C (b) and 900°C (c).

Therefore, comparatively lower performance at 600°C can be attributed to the lower amount of surface oxygen released. Similarly, at 750°C structural stability is quite evident from the SEM images and the diminished performance during the long-term run can be attributed to the phase changes occurring during cycling. Loss of microstructure and porosity to some extent was clearly visible from the high temperature SEM images obtained at 900°C. Since largest oxygen release/uptake amounts for prolonged duration was observed at this temperature, it can be concluded that the lack of stability is not due to carbon deposition and sintering issues. Instead the composition and oxygen release capacity of the phase obtained after the first redox cycle seems to determine the overall stability and performance of

$CaMnO_3$. Thus, regardless of the higher extent of sintering and structural changes observed, the variations in the oxidation state of manganese determined the redox stability and hence the efficiency in the long-term experiments.

SEM images were obtained for all the materials recovered after performing the redox cycling tests. Two representative regions were observed and were studied using EDS. Since the distribution of Mn and Ca were found to be uniform in all the materials, the focus was to determine the variations in surface oxygen content. No significant variations in the particle size and surface structure were observed for the material cycled at 600°C (Figure 3.10). Inter-particle pores were clearly visible to a large extent. Elemental mappings indicate a homogeneous distribution of the Ca, Mn and O throughout the surface, similar to fresh $CaMnO_3$.

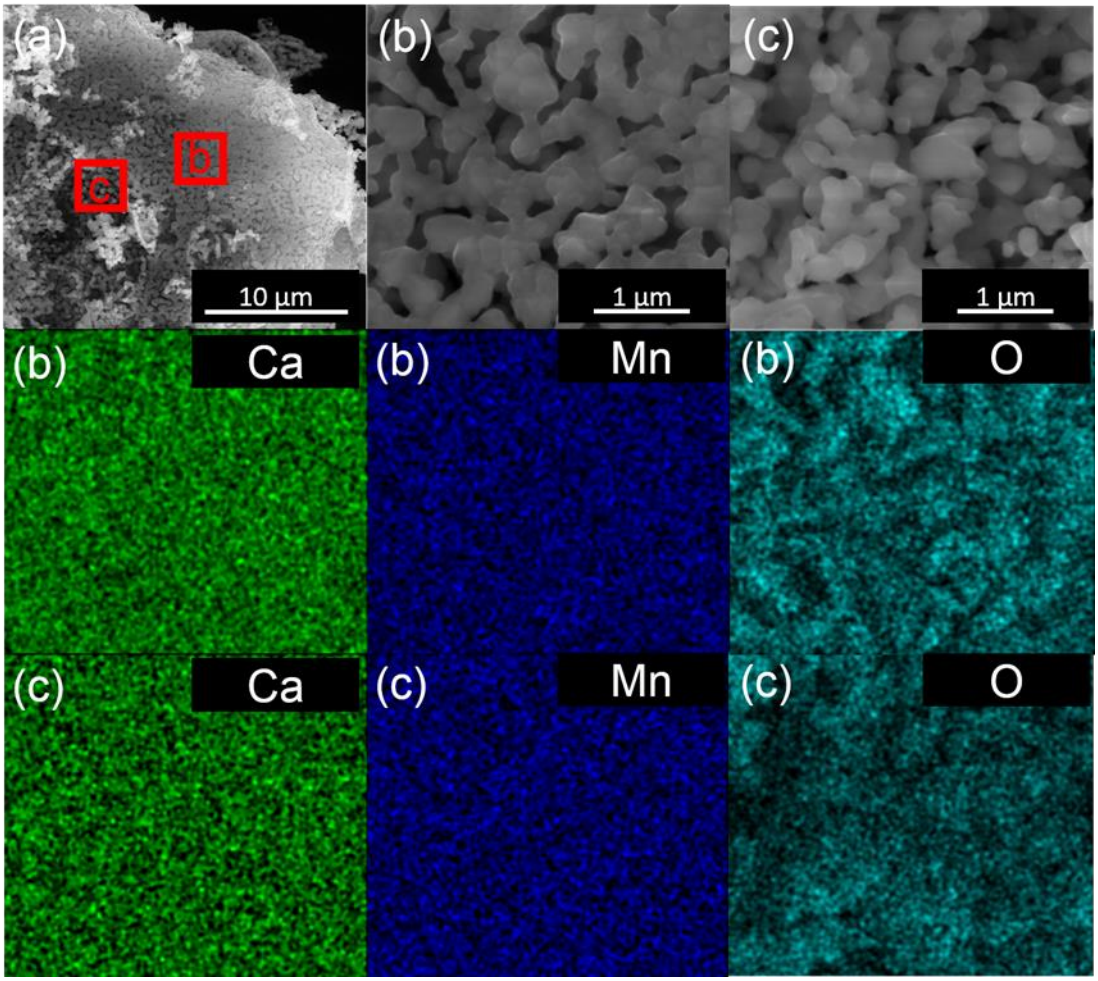

Figure 3. 10 SEM images of $CaMnO_3$ recovered after one redox cycle at 600°C. Elemental mappings for the corresponding regions are shown for Ca, Mn and O.

Clearly, the phase, surface structure and elemental distribution is not affected and hence a consistent redox performance was observed during 15 cycles at 600°C, as evident from Figure 3.11. These results are in agreement with the fact that the perovskite structure is maintained, as evident from the XRD pattern.

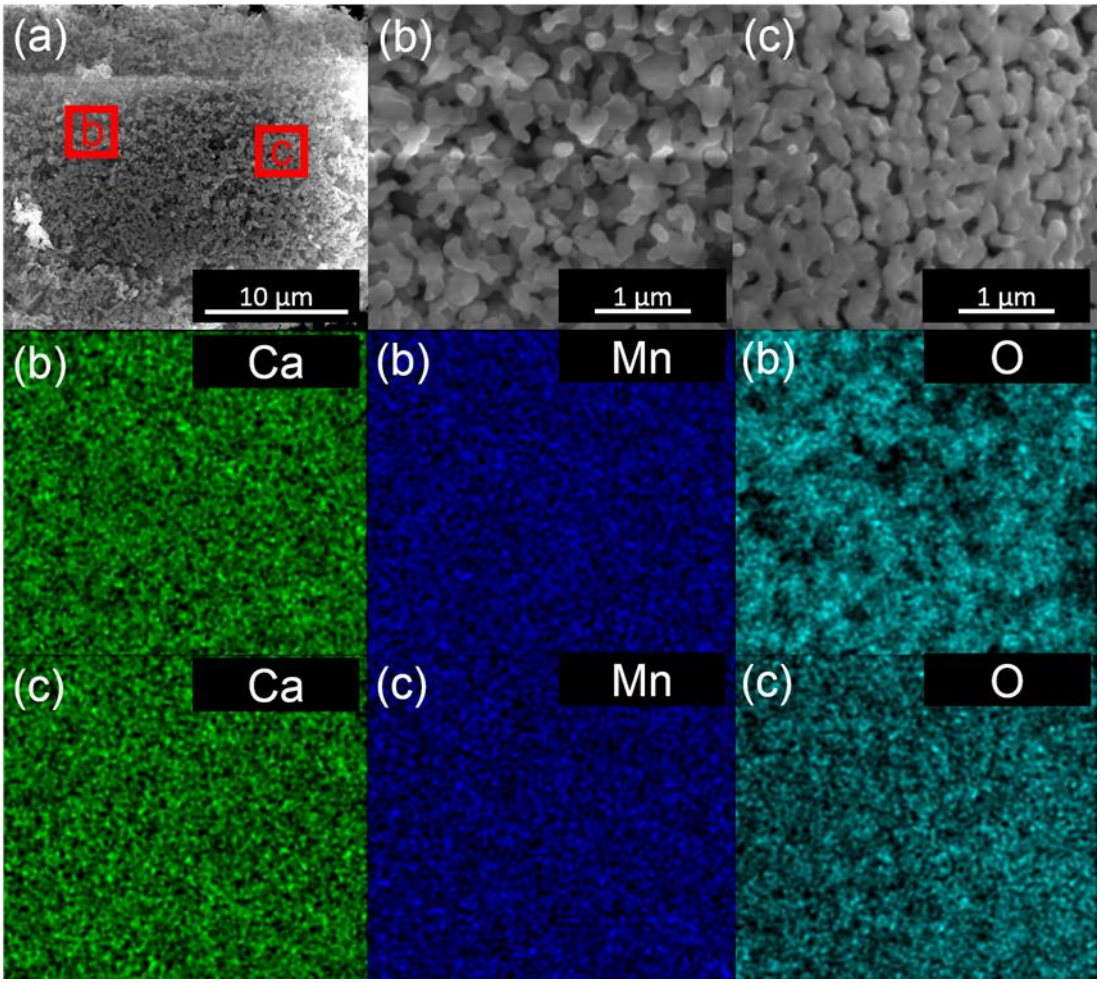

Figure 3. 11 . SEM images of $CaMnO_3$ recovered after 15 redox cycles at 600°C. Elemental mappings for the corresponding regions are shown for Ca, Mn and O.

Further, sintering was observed to some extent for the material cycled at 750°C and the elemental distribution remained uniform after one cycle (Figure 3.12). This implies that the composition remained intact after one redox cycle.

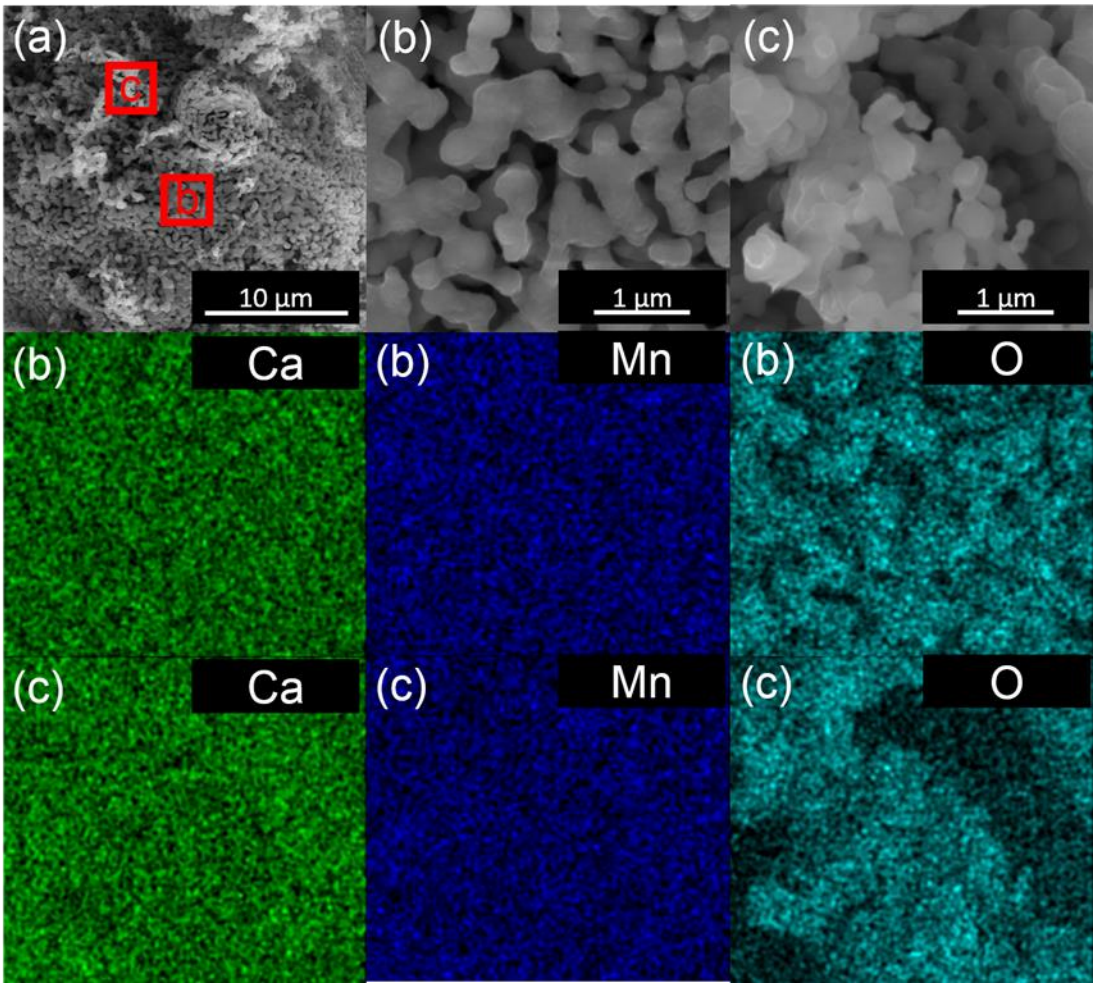

Figure 3. 12 SEM images of $CaMnO_3$ recovered after one redox cycle at 750°C. Elemental mappings for the corresponding regions are shown for Ca, Mn and O.

However, severe deactivation occurred for $CaMnO_3$ during the long term run for 15 cycles (Figure 3.13). Particle agglomeration was observed from the SEM images and elemental mapping clearly indicated surface oxygen deficiency in some regions for the material recovered after 15 cycles. These results agree well with the XRD pattern showing the complete collapse of perovskite structure resulting in the formation of a mixture of $CaMnO_{2.5}$ and $CaMnO_3$. Melting to some extent was evident in the surface region of the material recovered after long term cycling tests. However, the inner regions were found to maintain

their original porous architecture. It is to be noted that the observed oxygen release and uptake was much higher than what is obtained at 600°C.

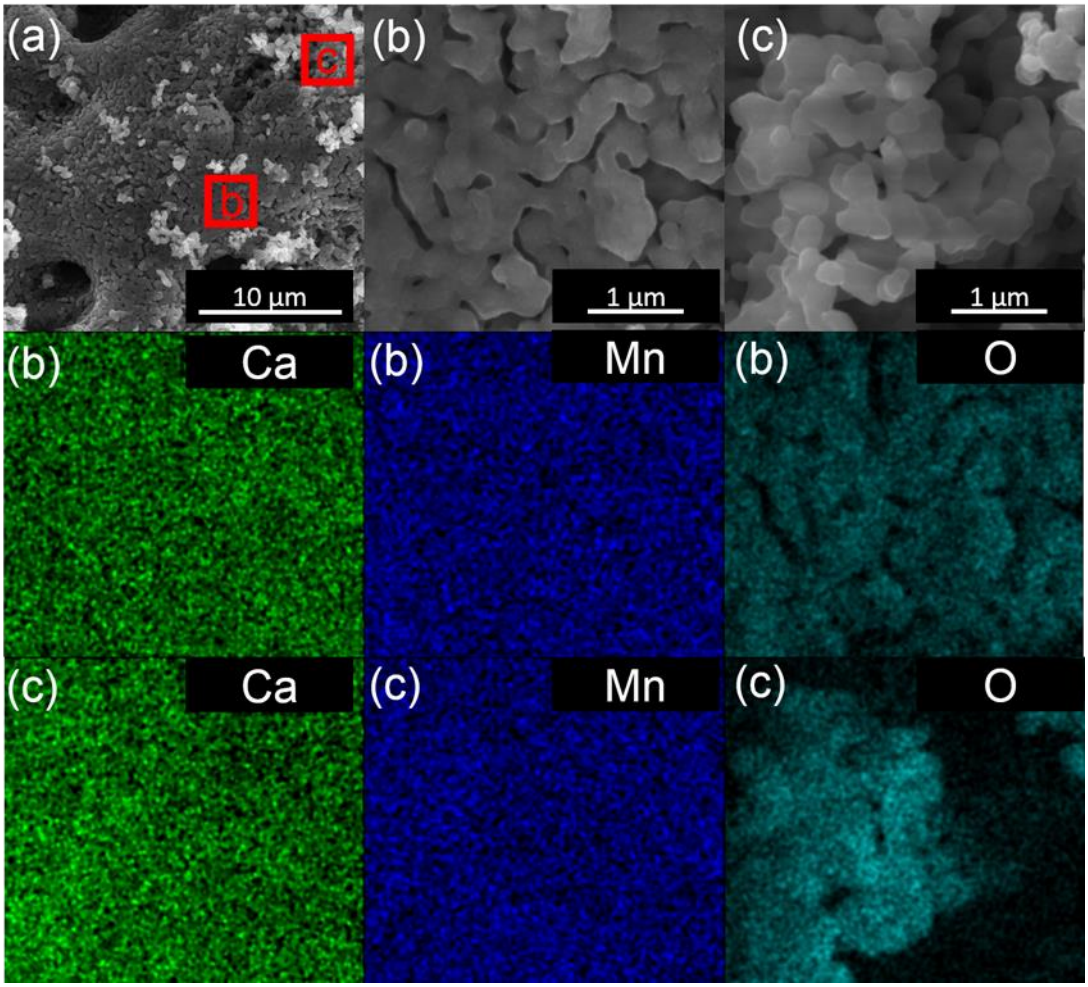

Figure 3. 13 SEM images of $CaMnO_3$ recovered after 15 redox cycles at 750°C. Elemental mappings for the corresponding regions are shown for Ca, Mn and O.

At 900°C, largely agglomerated particles were observed for the materials recovered after one cycle (Figure 3.14).

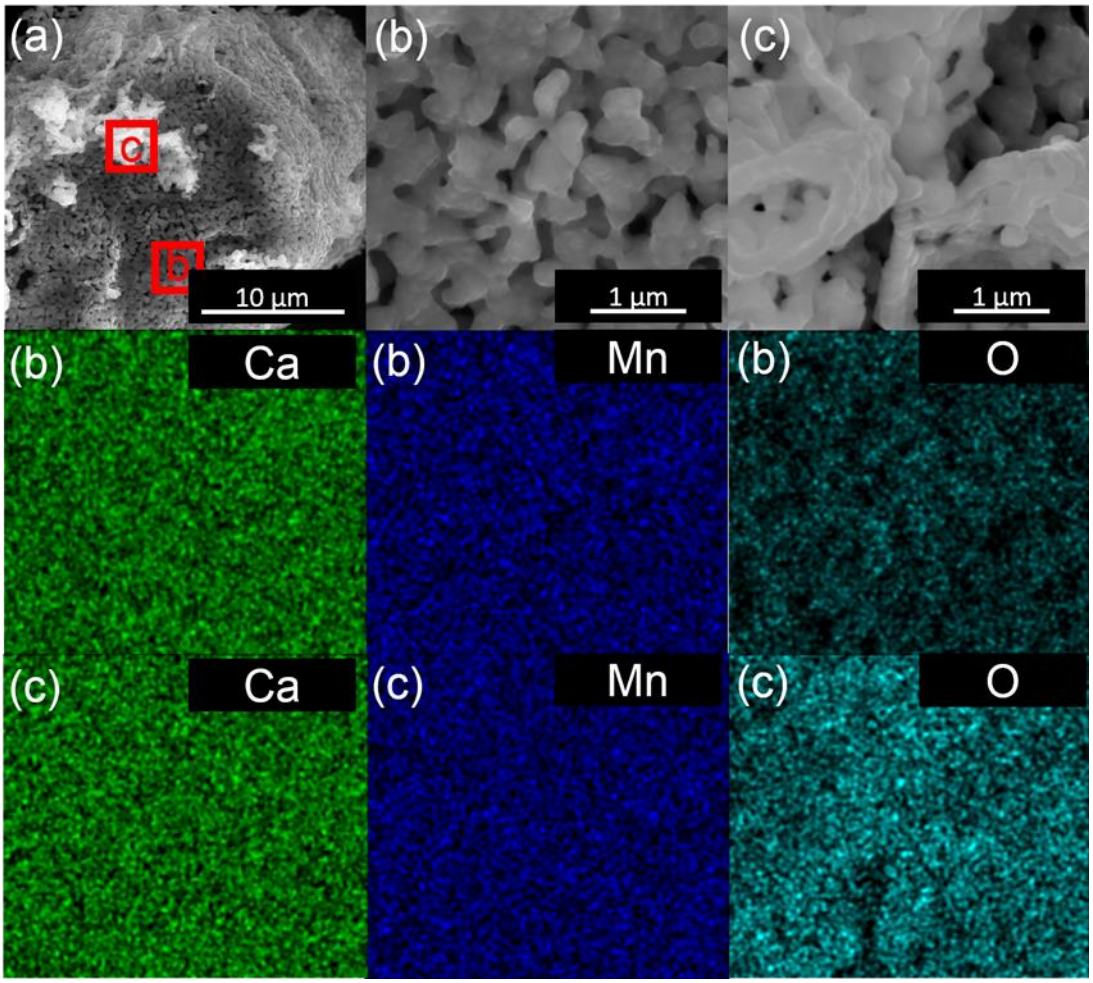

Figure 3. 14 SEM images of $CaMnO_3$ recovered after one redox cycle at 900°C. Elemental mappings for the corresponding regions are shown for Ca, Mn and O.

Further enhancement of this agglomeration was not visible after 15 cycles. Interestingly, two regions one having oxygen distribution similar to fresh $CaMnO_3$ and one oxygen deficient region, were observed (Figure 3.15). This oxygen deficient region can be attributed to $CaMnO_{2.5}$ as observed from the XRD pattern.

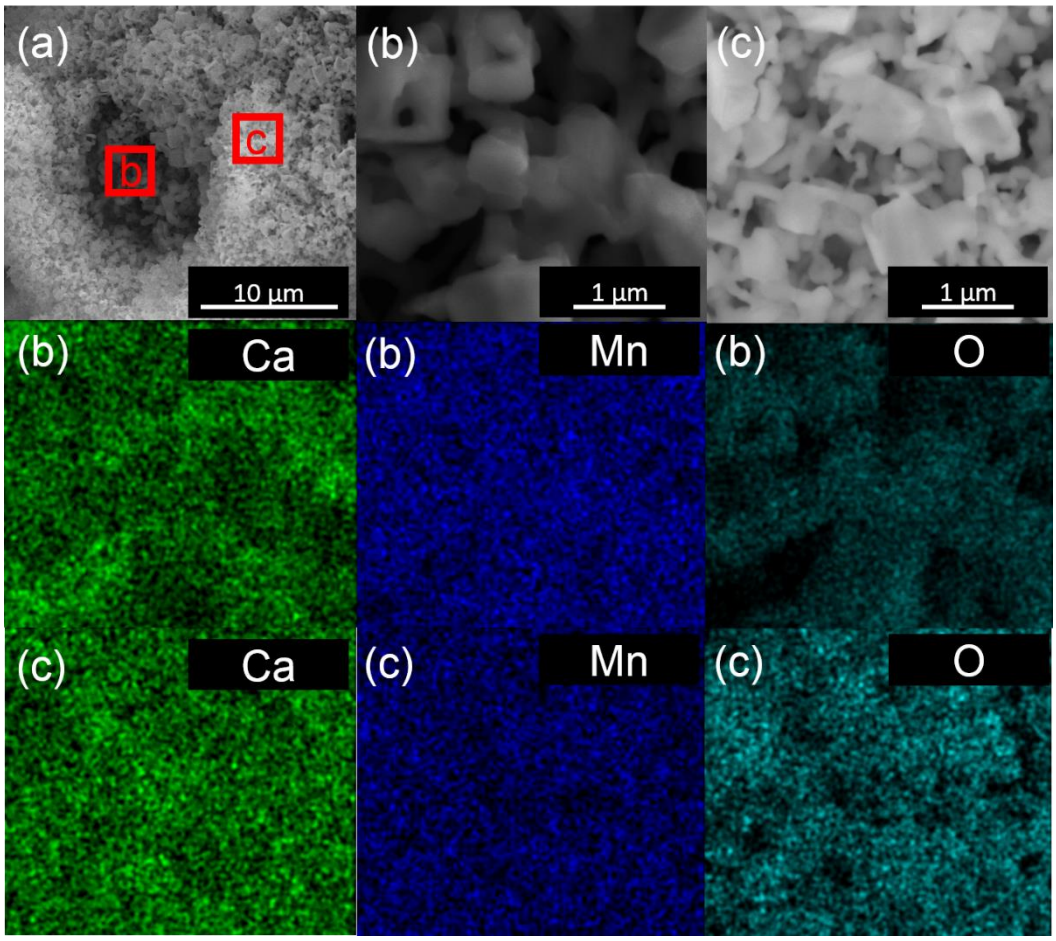

Figure 3. 15 SEM images of $CaMnO_3$ after 15 redox cycles at 900°C. Two different regions were observed indicating the presence of oxygen deficiency

Regarding applications involving fuel production as in solar thermochemical process, utilization of CO_2 as an oxidant seems to be more realistic. However, in this case, additional issues such as slow kinetics, carbonate formation, etc, needs to be overcome. Specifically, for Ca-based compositions chances are quite high for the formation of carbonates in presence of CO_2. For example, ex-solution of Ca from $CaMnO_3$ is quite likely during reduction and this Ca cannot be accommodated back into the perovskite lattice in case of carbonate formation. Thus, further optimization is inevitable to stabilize the perovskite structure. We believe that this can be achieved by partially substituting with cations less prone to

carbonation. Also, such cationic substitutions could either enhance the low temperature redox performance or can resist the undesired phase variations at high temperatures.

3.5 Conclusion

In conclusion, the isothermal redox properties of perovskite structured $CaMnO_3$ was studied. Preliminary investigations performed with CH_4 as the reducing agent and O_2 as the oxidizing agent (as in CLC), demonstrates that this material has promising potential. Specifically, oxygen release and uptake were observed for $CaMnO_3$ at a temperature as low as 600°C. Perovskite phase was found to be stable at 600°C from wide angle XRD patterns before and after cycling. Redox performance was in agreement with the state-of-the-art materials at higher temperatures. The structural variations during cycling experiments were probed by conducting high temperature SEM analysis and the results indicate that structural changes were not observed at lower temperatures until 750°C. Interestingly, sintering observed at 900°C does not affect the performance, exhibiting consistent oxygen release/uptake values for 15 cycles. Temperature and the related phase changes determined the redox performance of these materials.

CHAPTER 4: B-SITE SUBSTITUTION EFFECT ON $CaMnO_3$ REDOX PROPERTIES

4.1 Introduction

In last few decades, thermochemical redox cycle technologies have drawn extensive interest among scientists for their promising applications in aspects including green energy generation as well as CO_2 capture processes. Traditionally, the desired thermochemical routes were considered to be composed of two steps: a high temperature endothermic step, where partial reduction would take place in the non-stoichiometric metal oxide accompanying the evolution of oxygen gas; followed by a low temperature exothermic step, where the partially reduced metal oxide would be re-oxidized into its original form [110]. A step ahead, Muhich et al. demonstrated that isothermal redox cycles are more efficient than temperature-swing thermal cycles for time and energy losses occurring in the process of heating and cooling the metal oxide frequently [111]. Indeed, isothermal redox cycles are much more promising in time and energy efficiency aspect and the development of effective and stable redox materials is one of the key aspects for commercializing this technology. Also, the use of a reducing agent such as methane was previously proven to bring down the operating temperature to a large extent [112].

Among various redox materials studied so far, perovskites are unique owing to their superior redox kinetics at comparatively lower temperature [113]. A variety of possibilities can be achieved by the perovskite material in tuning its physiochemical properties by partially or completely substituting different metallic cations in the A and/or B-sites. In addition, they have the ability to retain their crystallographic structure during multiple high temperature redox cycles. The general reaction can be represented by the following equation:

$$ABO_3 \leftrightarrow ABO_{3-\delta} + \delta/2\ O_2 \quad (4.1)$$

The extent of anion non-stoichiometry and unusual cation oxidation states arising as a result of cation substitution significantly influence on the redox properties of these materials. Several perovskite structured oxides, especially the ones with doped cations on A and/or B-site, have demonstrated superior redox performance. Scheffe et al. showed that Sr doped $LaMnO_3$ has more reducible oxygen capacity than CeO_2 at 10^{-5} bar O_2 in the temperature range of 1250-1650°C for solar thermochemical splitting of H_2O and CO_2 [114]. Later on, McDaniel et al. demonstrated that doping $LaMnO_3$ with Sr and Al could also result into superior redox performance to CeO_2, with nine times H_2 yield and six times CO yield respectively when reduced at 1623 K and re-oxidized at 1273 K [115].

Out of various perovskite materials that have been studied so far, Ca based perovskite materials have been proven to exhibit huge potential for applications involving thermochemical redox cycles. A variety of pristine and A- and B-site substituted CaMn-based perovskites were previously studied for applications including air separation and solar fuel production [116, 117]. However fundamental insights are rather scarce, regarding the effect of B-site substitution on the redox performance of this interesting material. In this chapter, a series of CaMn-based perovskites Fe (5-50%) substitution in the B-site of the crystal structure were synthesized to study the effect of Fe when substituted on B-site of $CaMnO_3$ perovskite structural material.

4.2 Structure Analysis of Fe Substituted $CaMnO_3$ Materials

Fe substituted $CaMnO_3$ particles were synthesized by Pechini method and calcined at 900˚C. The detailed synthesis route was introduced in detail in Chapter 2.1. Whether a transition metal dopant can incorporate effectively into perovskite is heavily dependent on the nature of the specific element and structure of the parent material. In an ideal case, dopant can be dispersed into the pristine structure homogeneously and maintain the original perovskite structure. The XRD patterns of Fe doped perovskite materials with different doping concentrations are shown in Figure 4.1 (a). The numbers in the labels denoted the molar percentage of each element on B site of the perovskite oxides (For example, CMO is the short form of $CaMnO_3$, CFM37 is the short form of $CaFe_{0.3}Mn_{0.7}O_3$)

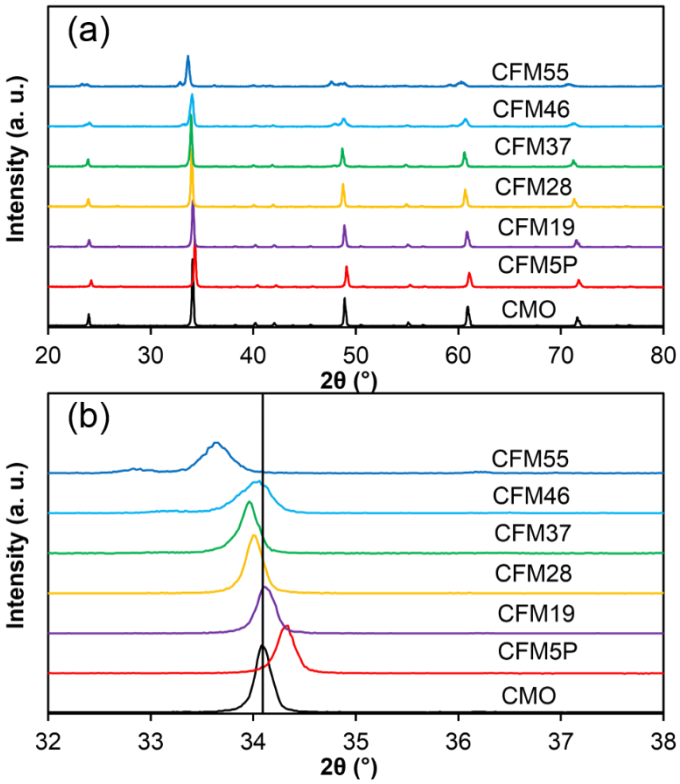

Figure 4. 1 (a) Wide angle XRD patterns of Fe doped $CaMnO_3$ perovskites (b) main peaks of XRD patterns

Identification of crystalline phases was performed by comparison with standard diffraction patterns (powder diffraction file PDF-2, International Center for Diffraction Data, ICDD) in MDI Jade 7. The results confirmed the presence of the doped $CaMnO_{3-\delta}$ perovskite phases in all the combinations. With lower dopant concentration, Fe (up to 20%) is effectively incorporated into the structure without any secondary phases. However, with higher dopant amount, minor amounts of impure phases started to form, indicated by peak segregation (23° and 33°) and diminishing (49° and 61°). Additionally, the incorporation of Fe into the B-site leads to a shift in the peaks, which can be clearly seen in the peak centred at 34°. This shift is a consequence of the distortion introduced by doping with larger cations. Cell refinement

was performed for pure phase materials (CMO, CFM5P, CFM19 and CFM28) to study the effect of dopant on lattice parameters by GSAS. The calculated lattice parameters for phase pure materials are summarized in Table 4.1, and fitting patterns of Rietveld refinement using the orthorhombic symmetry with Pnma space group can be found in the Appendix. It can be observed that both the lattice parameters and unit cell volume increase upon Fe-doping. Similar trend is also observed by Singh *et al.* [118] when they replaced Mn by Fe in composition $La_{0.8}Ca_{0.15}Na_{0.05}Mn_{1-x}Fe_xO_3$. Replacing Mn^{4+} in $CaMnO_3$ by other transition metal elements with other different sizes could result in lattice size variation. Since the ionic size of B-site species is following the order: $Mn^{4+}< Fe^{3+}< Mn^{3+}< Fe^{2+}$, the increase in the lattice constant is expected when doped by Fe especially with lower oxidation state.

Table 4. 1 Rietveld refinement lattice parameters and statistics for pure phase oxygen carriers

	CMO	**CFM5P**	**CFM19**	**CFM28**
Space group	Pnma	Pnma	Pnma	Pnma
a (Å)	5.2817(4)	5.2922(5)	5.3018(12)	5.3072(5)
b (Å)	7.45555(27)	7.4671(4)	7.4810(17)	7.4989(8)
c (Å)	5.27170(24)	5.2770(5)	5.2895(11)	5.3028(7)
Mn_{acc}	1.00	0.95	0.90	0.80
Fe_{acc}	0	0.05	0.10	0.20
Cell Volume ($Å^3$)	207.590(19)	208.531(30)	209.80(8)	211.04(4)
χ^2	1.3032	1.2800	1.3150	1.3635
R_p (%)	9.73	9.24	10.70	10.75
R_{wp} (%)	6.20	6.63	6.97	6.79

4.3 Surface Analysis of Fe Substituted $CaMnO_3$ Materials

The SEM images of prepared perovskites are shown in Fig. 4.2. All samples synthesized have randomly agglomerated particles and inter-particle porous structures. In addition, with increasing Fe dopant concentration, the particle size increases accordingly. Higher degree of agglomeration and shrinking pore size can also be observed as a trend. Theoretically, in application of CLC, lower pore volume could end up with more deficient redox performance due to the diffusion limit (less surface area) in the pore structure [119].

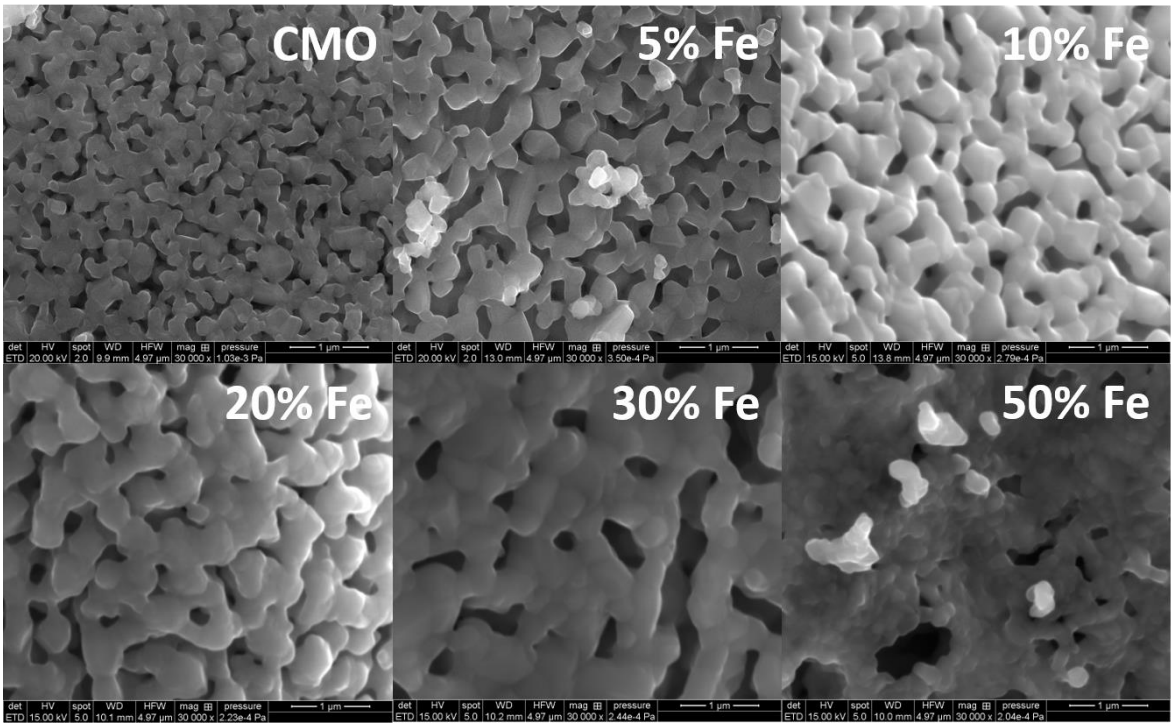

Figure 4. 2 SEM of Fe substituted CMO

EDS were performed to check the existence and distribution of interested the elements in the surface of synthesized phases. The element mapping of the $CaMn_{1-x}Fe_xO_3$ phases are shown

in Fig. 4.3. Irrespective of Fe substitution concentration, cation elements distributed homogeneously on the surface of the materials. No noticeable amount of element concentrated areas due to secondary phase formation were detected on the surface of the materials.

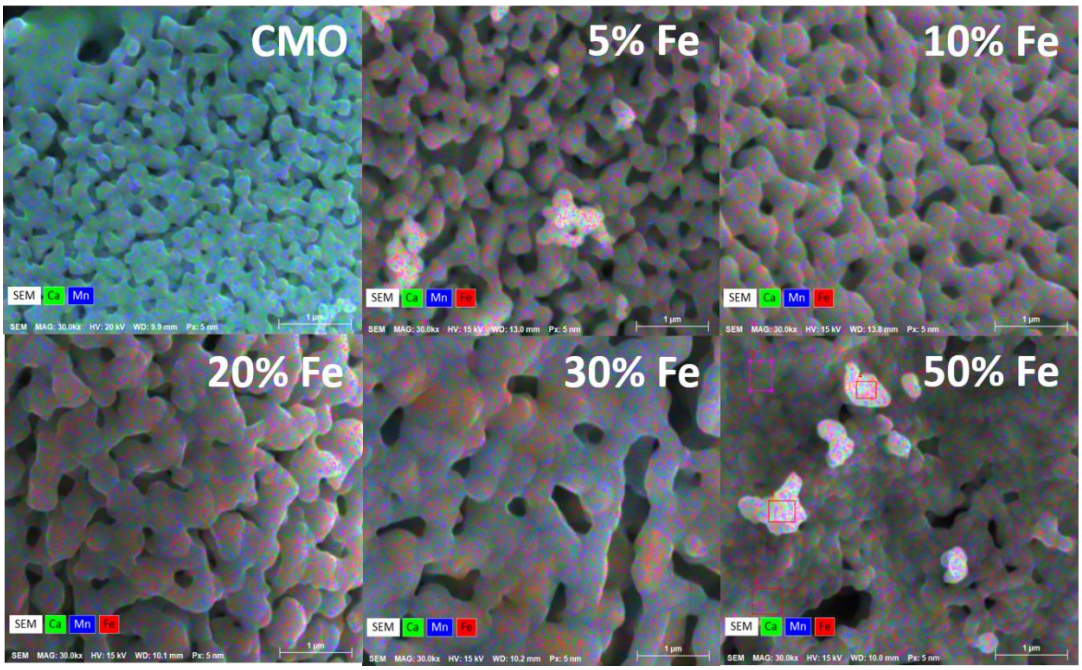

Figure 4. 3 Element Mapping of Fe substituted CMO

4.4 Isothermal Redox Performance in TGA

Addition of secondary metals into the A- or B-site of the perovskite would possibly improve the stability of the parent $CaMnO_3$ structure while obtaining more favorable redox properties. Pure $CaMnO_3$ is observed to decompose from perovskite structure into brownmillerite structures above 750°C in after redox cycles. Fig. 4.4 showed redox performance of pure and Fe doped $CaMnO_3$ under isothermal CLC condition at temperatures from 600°C to 900°C. All the materials exhibit reactivities at temperature as low as 600°C, which is rarely observed

for other oxygen carrier materials under CLC condition. Both pure and doped $CaMnO_3$ managed to retain perovskite structures after a full cycle at 600°C and 750°C. At 900°C, however, only doped samples could resist transforming into brownmillerite structure ($ABO_{2.5}$). This structure is more thermodynamically stable at elevated temperatures (> 750° C) under CLC conditions as observed in Chapter 4. In addition, the formation brownmillerite phases can diminish the oxygen transporting capacity permanently due to their difficulty to regenerate back to the perovskite structure in air under temperatures typical of chemical looping systems. Fe doped on B-site of the perovskite has significant impact on the redox properties of $CaMnO_3$, where both perovskite structure stability and the redox performance were enhanced simultaneously. Interestingly, the effect of Fe on improving the redox performance is highly dependent on the doping concentrations and experimental temperatures. At 600°C, CFM5P almost double the reduction extent compared to CMO, with oxygen carrying capacity (Ro) of 3.5%. The reduction extent of the materials with increasing Fe doping concentration start to drop accordingly. However, for materials with over 40% dopant concentration, the material redox performance is lower even compared to pure $CaMnO_3$. This behavior can be attributed to two factors. Firstly, as the impure phases formed as observed in XRD patterns, which has much lower or no oxygen transporting capacity compared to perovskite compositions at CLC operating conditions. Also, the materials with over 30% of Fe doping concentration has much less pore structure and high extent of particle agglomerations as seen in Figure 4.2. The unfavored morphology could help hider the performance of the materials in redox cycles. When the temperature reached 750°C and 900° C, the iron doped material undertook approximate same level of oxygen release, which is

around the thermotical maximum value for the perovskite to form rock-salted structures ($CaMnO_2$).

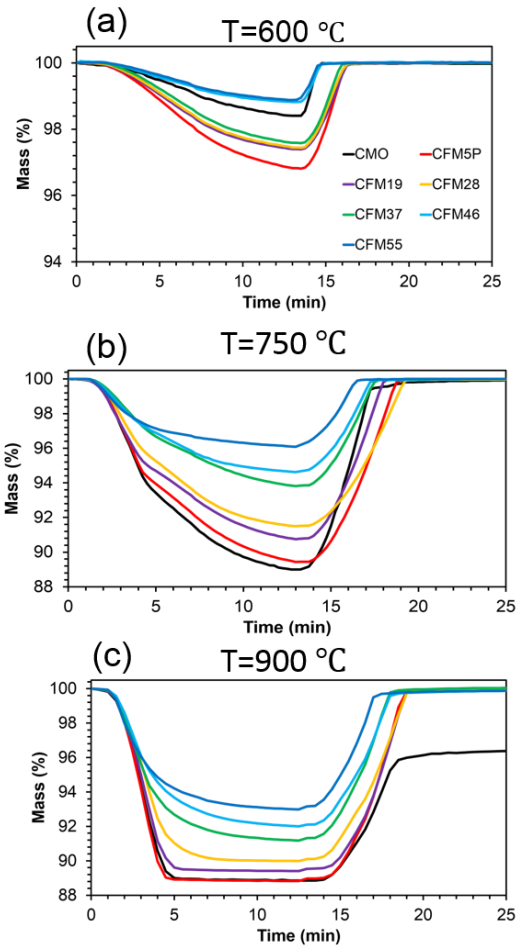

Figure 4.4 Isothermal redox profiles of pure and various Fe doped $CaMnO_3$ at selected temperatures (a) T=600°C, (b) T=750°C, and (c) T=900°C

Carbon deposition resulting from CH_4 decomposition during the reduction step is one major issue that can hinder the long-term performance of perovskites during redox cycling. Also, long-term stability of the materials as oxygen carriers is essential for CLC system to keep the process running without replenishing the oxygen carriers frequently. On this regard, multi-redox cycle experiments with 10% methane and 50% air were conducted for the phase pure

materials (CMO, CFM5P, CFM19 and CFM 28) to examine carbon deposition problems and material stabilities under long term redox conditions. Fig. 4.5 presents 15 redox cycles TGA profiles of pure phase Fe-doped $CaMnO_3$ at 600°C to 900°C with undoped $CaMnO_3$ as comparison.

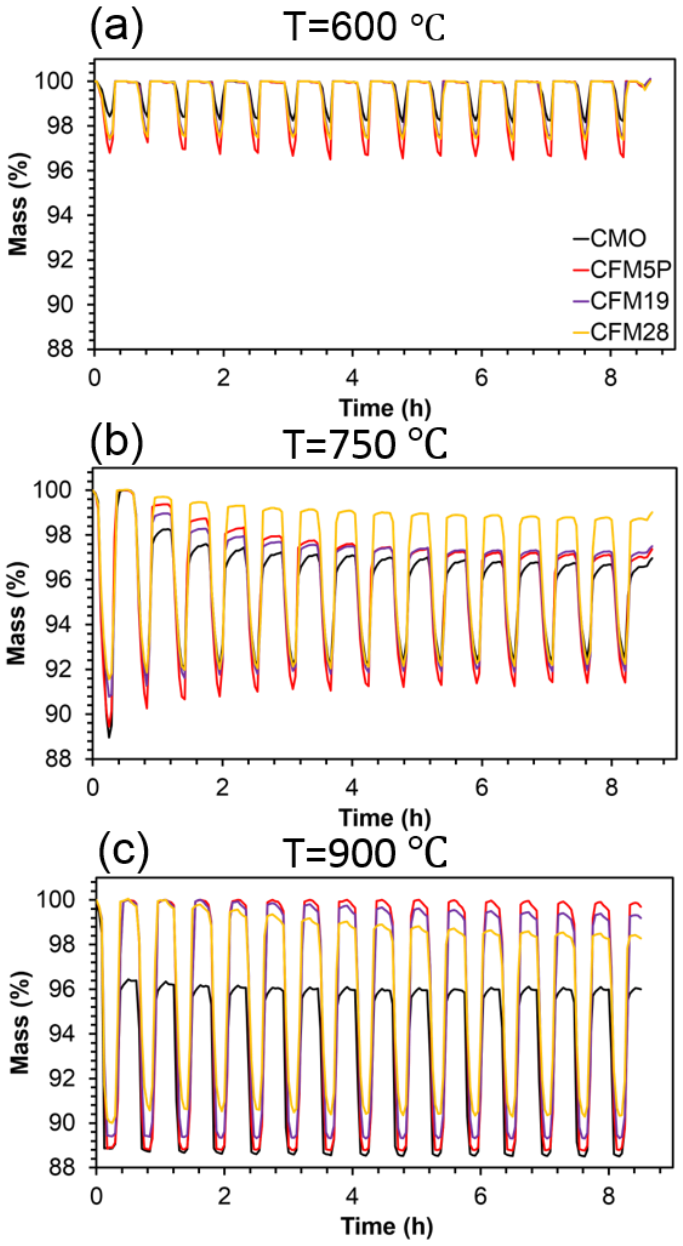

Figure 4.5 15 redox cycle TGA profiles of pure and various Fe doped $CaMnO_3$ at selected temperatures (a) T=600°C, (b) T=750°C, and (c) T=900°C

As Figure 4.6 shows, the long term redox performance of the selected materials is highly dependent on the reaction temperatures. Fe substitution tailored the stability of $CaMnO_3$ in different extent according to various doping concentration. All the tested materials exhibit little or no deactivation, showing stable performance at 600°C. However, when temperature was increased above 750°C, some of the materials demonstrate steady decay in the amount of released oxygen as a function of time. This phenomenon has been widely observed for the perovskite-type materials and is reported in literatures [120-122]. In addition, all Fe doped materials show enhanced stability and oxygen carrying capacity at each temperature. Especially for CFM5P, which possesses highest redox extent and stability at 600°C and 900°C. In the medium temperature (750°C), however, CFM28 demonstrated strongest resistance of the transforming perovskite structure into brownmillerite. The amounts of oxygen released from materials tested in long term experiments are shown in Table 4.2.

Table 4. 2 Oxygen released ($mmol.g^{-1}$) of prepared perovskites during various redox conditions

Material	**Cycle**	**600°C**	**750°C**	**900°C**
CMO	1 cycle reduction	0.4993	3.4399	3.4836
CMO	15 cycles reduction	0.5507	1.3094	2.2937
CFM5P	1 cycle reduction	0.9920	3.3021	3.4923
CFM5P	15 cycles reduction	1.0594	1.7832	3.4287
CFM19	1 cycle reduction	0.8126	2.8930	3.3108
CFM19	15 cycles reduction	0.8343	1.6640	3.1024
CFM28	1 cycle reduction	0.7545	2.6577	3.1273
CFM28	15 cycles reduction	0.8105	2.0406	2.5010

It can be clearly seen that at 600°C all the materials release slightly more oxygen at the 15th cycle compared to the first one, which means the perovskite structure is stable at this operating condition regardless of doping concentration. Also, the materials got more activated along with cycling numbers. Especially for CFM5P, it can be observed that this material has superior reduction extent compared to other counterparts. 5% doping concentration increased the performance to the largest extent. However, the performance decreased even with further efforts to incorporate more Fe on B-site. These results are in accordance with Wang and co-workers, who found that the addition of Fe can have either a promoting or a suppressing effect on catalytic steam reforming of tars depending on the added contrition [123]. Based on size effect theory proposed by Imanieh *et al.*, the oxygen capacity of the perovskite structured materials can be related to ionic motion mechanism. When Mn^{4+} was replaced by larger cations, it created expanded pathways for oxygen to be released/uptaken. As a result, more Fe doping should result into more oxygen transportation in redox cycles, which does not match the experimental results obtained [124]. Another theory proposed by Liu et al. stated that transition metal species on B-site has huge impact on oxygen transporting capacity based on their electronegativity difference [125]. By this theory, when more Fe (electronegativity = 1.83) replacing Mn (electronegativity = 1.55), the smaller difference between oxygen (electronegativity = 3.44) makes the bond more difficult to be broken. In this way, more Fe doping should result into less oxygen transportation capacity of the material. Based on the results obtained, the combination of these two explanations could be used to explain the observed behaviors. With doping amount less than 5%, size effect dominates, while electronegativity effect dominates with higher doping concentration.

At 750°C, the oxygen carrying capacity (R_O) of all the materials dropped gradually over the cycles. However, more Fe concentration on B-site seem to resist the perovskite structure transformation. At 900°C, CFM5P has excellent performance compared to undoped $CaMnO_3$ and materials with higher doping concentration. It can be concluded that Fe improved the stability and redox performance of $CaMnO_3$ at all the tested temperatures. However, the redox improvement behavior is a function of both doping concentration and experimental temperature. At 600°C and 900 °C, low Fe dopant (5%) has the best performance, while in the medium temperature (750°C), high Fe dopant enhanced the stability and redox extent most. It can be concluded that perovskite with small dopant concentration (CFM5P) successfully maintained the stability of undoped materials at elevated temperature (900°C). However, with more Fe amount presented, the combination showed more medium temperature stability. The potential reason is that higher Fe doping concentration may lead to less sintering resistance, consequently, less high temperature stability. In general, Fe successfully increased both oxygen carrying capacity and stability of CaMn-based materials simultaneously.

4.5 Conclusions

The present study investigated the effect of Fe doping on the redox properties of $CaMnO_3$ perovskite type oxygen carriers. The phase compatibility with $CaMnO_3$ parent structure, oxygen carrying capacity, phase stability, and CLC performance of these doped oxygen carriers were studied. Secondary phases were formed when dopant concentration was high. Fe was found to be fully compatible with the $CaMnO_3$ parent structure for up to 20%. Fe dopant was observed to significantly improve the phase stability of $CaMnO_3$ based oxygen carriers.

The redox properties of CaMn-based perovskite oxide oxygen carriers were found to be a function of both temperature and doping concentration. At 600°C, 5% Fe substitution exhibited best performance. CFM5P managed to double the oxygen carrying capacity compared to the undoped material (CMO) while maintaining stability of perovskite structure in multicycle experiments. However, at 750°C, all synthesized materials were observed to decompose as experiments proceeded. Among the samples, CFM28 showed superior stability and redox capacity. When the temperature was increased to 900°C, CFM5P presented stable redox behavior which can be fully re-oxidized back to perovskite form as well as high oxygen carrying capacity which reached maximum theoretical value between perovskite (ABO_3) and brownmillerite ($ABO_{2.5}$) structures. Potential reasons on explaining the effect of temperature and doping concentration on tailoring redox properties were also thoroughly discussed. CFM5P ($CaFe_{0.05}Mn_{0.95}O_3$) was proposed as the most promising perovskite oxygen carrier candidate due to its overall performance.

CHAPTER 5: CONCLUSIONS AND PERSPECTIVES

5.1 Conclusions

Materials with redox cycling properties have drawn extensive research attention and have found applications in many clean energy sections. In this thesis, CaMn-based perovskites were investigated in CLC processes for inherent CO_2 capture purpose. The materials were synthesized using Pechini method. Detailed preparation procedure was summarized. Studies of finding the lowest possible calcination temperature were carried out. 900°C was determined as the optimum calcination temperature for pure crystalline materials formation indicated by XRD patterns obtained of the materials calcined at different temperatures.

Comprehensive characterization techniques including XRD, SEM and EDS were utilized to study the composition and morphology of the synthesized materials. In cases of probing phase and structural changes of $CaMnO_3$ during redox cycles, the sample was characterized after several stages of reactions. The results were used to correlate observations from weight loss/gain during redox reactions in TGA at various temperatures (600-900°C).

The sample $CaMnO_3$ was first examined under one redox cycle under various concentration of methane (10% - 30%) and 50% of air. The TGA profiles and XRD patterns indicated that the material could retain its perovskite structure at 600°C. However, when the temperature was increased above 750°C, the material was reduced into rock-salt type ($CaMnO_2$). Re-oxidation at 750°C and 900 °C resulted into different compositions. At 750°C, the material remained perovskite after one redox cycle, while the phase was transformed into mixture of $CaMnO_{2.5}$ and $CaMnO_3$ at 900°C. Information obtained by SEM and EDS also confirmed the observed phase and structural evolution during the redox experiments. In addition, the

material showed resistance to the deactivation by sintering as indicated by high temperature SEM.

Moreover, multicycle experiments were carried out in TGA to study the performance of $CaMnO_3$ in CLC during longer operating conditions. The results showed that the material showed high stability at 600°C. However, the sample gradually lost its perovskite structure during cycling at 750°C. At 900°C, the phase transition was stable between $CaMnO_2$ and $CaMnO_{2.5}$. The residual samples after experiments were characterized by XRD, SEM and EDS in order to evaluate their changes after reduction and oxidation processes during multicycle experiments. In conclusion, perovskite structure of $CaMnO_3$ is only stable at temperature below 750°C. At elevated temperatures, brownmillerite structured CaMn-based oxide has ($CaMnO_{2.5}$) shown higher thermodynamic stability.

After probing the phase and structure evolution of base material, effect of B-site substitution with Fe investigated aiming at tailoring the redox properties of $CaMnO_3$. Different concentration of Fe (5% - 50%) was doped to replace Mn. XRD patterns revealed that materials with doping concentration more than 30% cannot incorporate into perovskite structure completely. High substitution concentration resulted into secondary phases formation. Moreover, the crystalline size is increasing with doping concentration since Fe^{3+} and Fe^{2+} has larger ionic size compared to Mn^{4+}. The pure phase doped CaMn-based perovskite oxides (CFM5P, CFM19 and CFM 28) were examined for their redox in a TGA at same experimental conditions with the undoped material.

Based on their redox performance in TGA, Fe can be concluded to increase the stability of $CaMnO_3$ perovskite structure as well as enhanced its oxygen capacity. Among all synthesized materials, perovskite with 5% doping concentration (CFM5P) has best overall performance, especially at high temperature (900°C). The possible reasonings of Fe effect in improving $CaMnO_3$ performance were also discussed in detail.

5.2. Suggestions for Future Work

The suggested recommendations for future work are as follows:

1. In this study, TGA was used as the main equipment for investigating redox behavior of materials. To obtain properties of the oxygen carrier such as attrition and agglomeration, experiments in a fluidized bed reactor with perovskite pellets are recommended.

2. Also, a flue gas detector such as (Fourier-transform infrared spectroscopy) FTIR is recommended to be installed with TGA to further understand the performance of the studied materials in CLC application.

3. In this thesis, efforts were focused on studying the effect of B-site substitution with Fe. Other transition metals including Co, Ni, Cu on B-site substitution or alkaline earth metal including Sr, Y, La on A-site substitution could be investigated to further enhance the redox performance of $CaMnO_3$.

Reference

[1] L. Nalbandian, A. Evdou and V. Zaspalis, La1-xSrxMyFe1-yO3-δ perovskites as oxygen-carrier materials for chemical-looping reforming, International Journal of Hydrogen Energy. 2011, 36, 6657-6670.

[2] J. R. Scheffe, A. Steinfeld, Thermodynamic analysis of cerium-based oxides for solar thermochemical fuel production, Energy & Fuels. 2012, 26 (3), 1928–1936.

[3] Q. Jiang, J. Tong, G. Zhou, Z. Jiang, Z. Li and C. Li, Thermochemical CO2 splitting reaction with supported LaxA1-xFeyB1-yO3 (A = Sr, Ce, B = Co, Mn; $0 \leq x, y \leq 1$) perovskite oxides, Solar Energy. 2014, 103, 425-437.

[4] Z. Shao and S. M. Haile, A high-performance cathode for the next generation of solid-oxide fuel cells, Nature. 2004, 431(7005). 170-173.

[5] F. Dong, D. Chen, Y. Chen, Q. Zhao and Z. Shao, La-doped BaFeO3-δ perovskite as a cobalt-free oxygen reduction electrode for solid oxide fuel cells with oxygen-ion conducting electrolyte, Journal of Materials Chemistry. 2012, 22 (30), 15071-15079.

[6] B. Moghtaderi, Application of chemical looping concept for air separation at high temperatures, Energy Fuels. 2009, 24, 190-198.

[7] J. Vieten, B. Bulfin, F. Call, N. Lange, M. Schmucker, A. Francke, M. Roeb and C. Sattler, Perovskite oxides for application in thermochemical air separation and oxygen storage, Journal of Materials Chemistry A. 2016, 4, 23652-13659.

[8] A. Abad, J.Adánez, F. García-Labiano, L. F. de Diego, P.Gayán and J. Celaya, Mapping of the range of operational conditions for Cu-, Fe-, and Ni-based oxygen carriers in chemical-looping combustion, Chemical Engineering Science. 2007, 62, 533 – 549.

[9] M. Ishida, H. Jin, A new advanced power-generation system using chemical-looping combustion, Energy, 1994, 19 (4), 415-422.

[10] T. Mattisson, A. Lyngfelt and P. Cho, The use of iron oxide as an oxygen carrier in chemical-looping combustion of methane with inherent separation of CO2, Fuel. 2001, 80, 1953-1962.

[11] Climate Change 2013: The Physical Science Basis, IPCC, 2016. Available in https:// http://www.climatechange2013.org/images/report/WG1AR5_ALL_FINAL.pdf

[12] G. A. Florides and P. Christodoulides, Global warming and carbon dioxide through sciences, Environment International. 2009, 35 (2), 390-401.

[13] M. M. Hossain, H. I. de Lasa, Chemical-looping combustion (CLC) for inherent CO2 separations—a review, Chemical Engineering Science. 2008, 63 (18), 4433-4451.

[14] M. Ishida, D. Zheng, T. Akehata, Evaluation of a chemical-looping-combustion power-generation system by graphic exergy analysis, Energy, 12 (1987), 147-154.

[15] A. B. Harichandan, T. Shamim, Effect of fuel and oxygen carriers on the hydrodynamics of fuel reactor in a chemical looping combustion system, Journal of Thermal Science and Engineering Applications. 2014, 6 (4), 41013-41021.

[16] M. Ishida, H. Jin, A novel chemical-looping combustor without NOx formation, Industrial & Engineering Chemistry Research. 1996, 35, 2469-2472.

[17] P. Furler, J. R. Scheffer, A. Steinfeld, Syngas production by simultaneous splitting of H2O and CO2 via ceria redox reactions in a high-temperature solar reactor, Energy Environmental Science. 2012, 5, 6098−6103.

[18] W. T. Gibbons, L. J. Venstrom, R. M. De Smith, J. H. Davidson, G. S. Jackson, Ceria-based electrospun fibers for renewable fuel production via two-step thermal redox cycles for carbon dioxide splitting, Physical Chemistry Chemical Physics. 2014, 16, 14271−14280.

[19] Y. Hao, C. K. Yang, S. M. Haile, High-temperature isothermal chemical cycling for solar-driven fuel production, Physical Chemistry Chemical Physics. 2013, 15, 17084−17092.

[20] P. Furler, J. R. Scheffer, D. Marxer, M. Gorbar, A. Bonk, U. Vogt, A. Steinfeld, Thermochemical CO2 splitting via redox cycling of ceria reticulated foam structures with dual-scale porosities, Physical Chemistry Chemical Physics. 2014, 16, 10503−10511.

[21] M. Ishida, H. Jin, T. Okamoto, Kinetic behavior of solid particles in chemical-looping combustion: suppressing carbon deposition in reduction, Energy & Fuels. 1998, 12, 223-229.

[22] J. Adanez, L.F. de Diego, F. Garcia-Labiano, P. Gayan, A. Abad, Selection of oxygen carriers for chemical-looping combustion, Energy & Fuels. 2004, 18, 371-377.

[23] Guo Q, Liu Y, Tian H. Recent Advances on preparation and characteristics of oxygen carrier particles. Industrial Research of Chemical Engineering. 2009, 1, 357-368.

[24] F. He, H. Li, and Z. Zhao, Advancements in development of chemical-looping combustion: A review, International Journal of Chemical Engineering. 2009, 2009, 1-16.

[25] J. Adanez, A. Abad, F. Garcia-Labiano, P. Gayan, L.F. de Diego, Progress in chemical-looping combustion and reforming technologies, Progress in Energy and Combustion Science. 2012, 38, 215-282.

[26] T. Mattisson, A. Jàrdnâs, A. Lyngfelt, Reactivity of some metal oxides supported on alumina with alternating methane and oxygen application for chemical-looping combustion, Energy & Fuels. 2003, 17, 643-651.

[27] P. Cho, T. Mattisson, A. Lyngfelt, Comparison of iron-, nickel-, copper- and manganese-based oxygen carriers for chemical-looping combustion, Fuel. 2004, 83, 1215-1225.

[28] L.F. de Diego, P. Gayan, F. Garcia-Labiano, J. Celaya, A. Abad, J. Adanez, Impregnated CuO/Al2O3 oxygen carriers for chemical-looping combustion: avoiding fluidized bed agglomeration, Energy & Fuels. 2005, 19, 1850-1856.

[29] S. R. Son, K. S. Go, and S. D. Kim, Thermogravimetric analysis of copper oxide for chemical-looping hydrogen generation, Industrial and Engineering Chemistry Research. 2009, 48 (1), 380–387.

[30] M. Johansson, T. Mattisson, A. Lyngfelt, Investigation of Fe2O3 with MgAl2O4 for chemical-looping combustion, Industrial and Engineering Chemistry Research. 2004, 43, 6978-6987.

[31] T. Mattisson, M. Johansson, A. Lyngfelt, Multicycle reduction and oxidation of different types of iron oxide particles—application to chemical-looping combustion, Energy & Fuel. 2004, 18, 628-637.

[32] P. Cho, T. Mattisson, A. Lyngfelt, Carbon Formation on Nickel and Iron Oxide-Containing Oxygen Carriers for Chemical-Looping Combustion, Industrial and Engineering Chemistry Research. 2005, 44, 668-676.

[33] Determination of the oxidation state for iron oxide minerals by energy-filtering TEM, U. Golla-Schindler, R. Hinrichs, O. Bomati-Miguel, A. Putnis, Micron, 2006. 37 (5), 473-477l.

[34] J. Zhang, Q. Guo, Y. Liu, and Y. Cheng, Preparation and characterization of Fe2O3/Al2O3 using the solution combustion approach for chemical looping combustion, Industrial and Engineering Chemistry Research. 2012, 51, 12773−12781.

[35] B.M. Corbella, J.M. Palacios, Titania-supported iron oxide as oxygen carrier for chemical-looping combustion of methane, Fuel. 2007, 86, 113-122.

[36] J. Adanez, A. Abad, F. Garcia-Labiano, P. Gayan, L.F. de Diego, Progress in chemical-looping combustion and reforming technologies, Progress in Energy and Combustion Science. 2012, 38, 215-282.

[37] E. R. Stobbe, B.A. de Boer, J. W. Geus, The reduction and oxidation behaviour of manganese oxides, Catalysis Today. 1999, 47, 161-167.

[38] Q. Zafar, A. Abad, T. Mattisson, B. Gevert, M. Strand, Reduction and oxidation kinetics of Mn3O4/Mg-ZrO2 oxygen carrier particles for chemical-looping combustion, Chemical Engineering Science. 2007, 62, 6556-6567.

[39] Q. Zafar, T. Mattisson, B. Gevert, Integrated hydrogen and power production with CO_2 capture using chemical-looping reforming redox reactivity of particles of CuO, Mn_2O_3, NiO, and Fe_2O_3 using SiO_2 as a support, Industrial and Engineering Chemistry Research. 2005, 44, 3485-3496.

[40] T. Mattisson, A. Jàrdnâs, A. Lyngfelt, reactivity of some metal oxides supported on alumina with alternating methane and oxygen application for chemical-looping combustion, Energy Fuels. 2003, 17, 643-651.

[41] Q. Zafar, T. Mattisson, B. Gevert, Redox investigation of some oxides of transition-state metals Ni, Cu, Fe, and Mn supported on SiO_2 and $MgAl_2O_4$, Energy Fuels. 2005, 20, 34-44.

[42] M. Johansson, T. Mattisson, and A. Lyngfelt, Investigation of Mn_3O_4 with stabilized ZrO_2 for chemical-looping combustion, Chemical Engineering Research and Design. 2006, 84, 807-818.

[43] A. Abad, T. Mattisson, A. Lyngfelt, M. Rydén, Chemical-looping combustion in a 300W continuously operating reactor system using a manganese-based oxygen carrier, Fuel. 2006, 85, 1174-1185.

[44] J. Adanez, L.F. de Diego, F. Garcia-Labiano, P. Gayan, A. Abad, Selection of oxygen carriers for chemical-looping combustion, Energy & Fuels, 2004. 18, 371-377.

[45] W. C. Chueh, C. Falter, M. Abbott, D. Scipio, P. Furler, S. M. Haile, A. Steinfeld, High-flux solar-driven thermochemical dissociation of CO_2 and H_2O using nonstoichiometric ceria, Science. 2010, 330 (6012), 1797–1801.

[46] N. M. Mogensen, G.A. Sammes, Tompsett, Physical, chemical and electrochemical properties of pure and doped ceria, Solid State Ionics. 2000, 129 (1–4), 63–94.

[47] G. J. VanHandel, R. N. Blumenthal, The temperature and oxygen pressure dependence of the ionic transference number of nonstoichiometric CeO_{2-x}, Journal of the Electrochemical Society. 1974, 121 (9), 1198–1202.

[48] R. Dieckmann, H. Schmalzried, Defects and cation diffusion in magnetite (i), Berichte der Bunsengesellschaft für physikalische Chemie. 1977, 81 (3), 344–347.

[49] S. Sajen, S. K. Singh, P. Mungse, S. Rayalu, K. Watanabe, G. Saravanan, N. Labhasetwar, Mechanically Stable Mixed Metal Oxide of Cu and Mn as Oxygen Carrier for Chemical Looping Syngas Combustion, Energy & Fuels. 2016, 30, 7596-7603.

[50] M. M. Hossain, H. I. de Lasa, Reactivity and stability of Co-Ni/Al_2O_3 oxygen carrier in multicycle CLC, AlChE Journal, 2007, 53 (7), 1817-1829.

[51] H. Jin, T. Okamoto, M. Ishida, Development of a novel chemical-looping combustion: synthesis of a looping material with a double metal oxide of CoO-NiO, Energy & Fuels. 1998, 12, 1272-1277.

[52] S. R. Son, S. D. Kim, Chemical-looping combustion with NiO and Fe_2O_3 in a thermo balance and circulating fluidized bed reactor with double loops, Industrial & Engineering Chemistry Research. 2006, 45, 2689-2696.

[53] R. Siriwardane, H. Tian, R. Simonyi, J. Poston, Synergetic effects of mixed copper-iron oxides oxygen carriers in chemical looping combustion, Fuel. 2013, 108, 319-333.

[54] F.S. Galasso, Structure, properties, and preparation of perovskite-type compounds, Pergamon Press. 1969.

[55] M. A. Peña, and J. L. G. Fierro, Chemical structures and performance of perovskite oxides, Chemical Reviews. 2001, 101 (7), 1981–2018.

[56] S. Sasaki, C. T. Prewitt, R. C. Liebermann, The crystal structure of $CaGeO_3$ perovskite and the crystal chemistry of the $GdFeO_3$-type perovskites, American Mineralogist. 1983, 68, 1189-1198, 1983.

[57] H. D. Megaw, Crystal structure of double oxides of the perovskite type, Proceedings of the Physical Society. 1946, 58, 133-152.

[58] B. C. Tofield, W. R. Scott, Oxidative nonstoichiometry in perovskites, an experimental survey; the defect structure of an oxidized lanthanum manganite by powder neutron diffraction, Journal of Solid State Chemistry. 1974, 10, 183-194.

[59] J. A. Alonso, M. J. Martínez-Lope, J. L. García-Muñoz, M. T. Fernández, Crystal structure and magnetism in the defect perovskite $LaNiO_{2.5}$, Physica B: Condensed Matter. 1997, 234-236, 18-19.

[60] M. M. V. Petrovic, J. D. Bobic, 2 – Perovskite and aurivillius: types of ferroelectric metal oxides, magnetic, ferroelectric, and multiferroic. Metal Oxides. 2018, 35-49.

[61] Z. Sarshar, F. Kleitz, Y. Lairing, S. Kaliaguine, Novel oxygen carriers for chemical looping combustion: $La_{1-x}Ce_xBO_3$ (B = Co, Mn) perovskites synthesized by reactive grinding and nanocasting, Energy & Environmental Science. 2011, 4, 4258-4270.

[62] M. Rydén, A. Lyngfelt, T. Mattisson, D. Chen, A. Holmen, E. Bjorgum, Novel oxygen-carrier materials for chemical-looping combustion and chemical-looping

reforming; $La_xSr_{1-x}Fe_yCo_{1-y}O_{3-\delta}$ perovskites and mixed-metal oxides of NiO, Fe_2O_3 and Mn_3O_4, International Journal of Greenhouse Gas Control. 2008, 2, 21-36.

[63] H. Leion, Y. Larring, E. Bakken, R. Bredesen, T. Mattisson, A. Lyngfelt, Use of $CaMn_{0.875}Ti_{0.125}O_3$ as oxygen carrier in chemical-looping with oxygen uncoupling, Energy & Fuels. 2009, 23, 5276-5283.

[64] A. Waindich, A. Möbius, M. Müller, Corrosion of $Ba_{1-x}Sr_xCo_{1-y}Fe_yO_{3-\delta}$ and $La_{0.3}Ba_{0.7}Co_{0.2}Fe_{0.8}O_{3-\delta}$ materials for oxygen separating membranes under oxycoal conditions. Journal of Membrane Science, 2009, 337, 182–187.

[65] T. Nagai, W. Ito, T. Sakon, Relationship between cation substitution and stability of perovskite structure in $SrCoO_{3-\delta}$-based mixed conductors, Solid State Ion. 2007, 177, 3433–3444.

[66] E. Juste, A. Julian, G. Etchegoyen, P.M. Geffroy, T. Chartier, N. Richet, Oxygen permeation, thermal and chemical expansion of (La, Sr) (Fe, Ga) $O_{3-\delta}$ perovskite membranes, Journal of Membrane Science. 2008, 319, 319, 185–191.

[67] M. Panneerselvam, K. J. Rao, Microwave preparation and sintering of industrially important perovskite oxides: $LaMO_3$ (M = Cr, Co, Ni), Journal of Materials Chemistry. 2003, 13, 596-601.

[68] B.L. Cushing, V.L. Kolesnichenko, C.J. O'Connor, Recent advances in the liquid-phase syntheses of inorganic nanoparticles, Chemical Reviews. 2004, 104, 3893-3946.

[69] H. Wang, Y. Cong, W. Yang, Oxygen permeation study in a tubular $Ba_{0.5}Sr_{0.5}Co_{0.8}Fe_{0.2}O_{3-\delta}$ oxygen permeable membrane, Journal of Membrane Science. 2002, 210, 259–271.

[70] P. Cousin, R. A. Ross, Preparation of mixed oxides: a review, Materials Science and Engineering: A. 1990, 130, 119–125.

[71] W. Haron, A. Wisitsoraat, S. Wongnaw, Nanostructured perovskite oxides – $LaMO_3$ (M=Al, Co, Fe) prepared by co-precipitation method and their ethanol-sensing characteristics, Ceramics International. 2017, 43(6), 5032-5040.

[72] M. P. Pechini, Method of preparing lead and alkaline earth titanates and niobates and coating method using the same to form a capacitor, U.S. Patent No. 3330697, 1967.

[73] R. D. Toro, P. Hernández, Y. Díaz, J. L. Brito, Synthesis of $La_{0.8}Sr_{0.2}FeO_3$ perovskites nanocrystals by Pechini sol–gel method, Materials Letters. 2013, 107, 231-234.

[74] K. R. Thampi, M.S. Rao, W. Schwarz, M. Grätzel, J. Kiwi, Preparation of $SrTiO_3$ by sol–gel techniques for the photoinduced production of H_2 and surface peroxides from water, Journal of the Chemical Society, Faraday Transactions. 1988, 1 (84), 1703-1712.

[75] O. Büchler, J. M. Serra, W. a Meulenberg, D. Sebold, H. P. Buchkremer, Preparation and properties of thin $La_{1-x}Sr_xCo_{1-y}Fe_yO_{3-\delta}$ perovskitic membranes supported on tailored ceramic substrates, Solid State Ionics. 2007, 178, 91–99.

[76] S. Kaliaguine, A. Van Neste, Process for synthesizing perovskites using high energy milling, U.S. Patent 6,017,504, 2000.

[77] S. Kaliaguine, A. Van Neste, V. Szabo, J.E. Gallot, M. Bassir, R. Muzychuk, Perovskite-type oxides synthesized by reactive grinding: Part I. Preparation and characterization, Applied Catalysis A: General. 2001, 209, 345-358.

[78] Z. Sarshar, F. Kleitzb, S. Kaliaguine, Novel oxygen carriers for chemical looping combustion: $La_{1-x}Ce_xBO_3$ (B = Co, Mn) perovskites synthesized by reactive grinding and nanocasting, Energy & Environmental Science. 2011, 4, 4258-4269.

[79] S. Royer, F. Bérubé, S. Kaliaguine, Effect of the synthesis conditions on the redox and catalytic properties in oxidation reactions of $LaCo_{1-x}Fe_xO_3$, Applied Catalysis A:

General. 2005, 282, 273-284.

[80] A. Lu, F. Schüth, Nanocasting: A Versatile Strategy for Creating Nanostructured Porous Materials, Advanced Materials. 2006, 18, 1793-1805.

[81] M. Tiemann, Repeated templating, Chemistry of Materials. 2008, 20 (3), 961-971.

[82] M. M. Nair, F. Kleitz, S. Kaliaguine, Kinetics of methanol oxidation over mesoporous perovskite catalysts, ChemCatChem. 2012, 4, 387-394.

[83] A. Rumplecker, F. Kleitz, E. Salabas, F. Schuth, Hard templating pathways for the synthesis of nanostructured porous Co_3O_4, Chemistry of Materials. 2007, 19 (3), 485-496.

[84] Y. Wang, J. Ren, Y. Wang, F. Zhang, X. Liu, Y. Guo, G. Lu, Nanocasted synthesis of mesoporous $LaCoO_3$ perovskite with extremely high surface area and excellent activity in methane combustion, Journal of Physical Chemistry C. 2008, 112 (39), 15293-15298.

[85] M. M. Nair, F. Kleitz, S. Kaliaguine, Pore structure effects on the kinetics of methanol oxidation over nanocast mesoporous perovskites, Chinese Journal of Catalysis, 2015, 36, 72, 0-0.

[86] J. Sunarso, S. Baumann, J. M. Serra, W. A. Meulenberg, S. Liu, Y. S. Lin, Mixedionic–electronic conducting (MIEC) ceramic-based membranes for oxygen separation, Journal of Membrane Science. 2008, 320, 13–41.

[87] T. R. N. Kutty, R. Vivekanandan, Preparation of $CaTiO_3$ fine powder by the hydrothermal method, Materials Letters, 1987, 5, 79–83.

[88] T. Zhang, C. G. Jin, T. Qian, X. L. Lu, J. M. Bai, X. G. Li, Hydrothermal synthesis of single-crystalline $La_{0.5}Ca_{0.5}MnO_3$ nanowires at low temperature, Journal of Materials Chemistry, 2004, 14, 2787–2789.

[89] P. Chai, X. Liu, Z. Wang, M. Lu, X. Cao, and J. Meng, Tunable Synthesis, Growth Mechanism, and Magnetic Properties of $La_{0.5}Ba_{0.5}MnO_3$, Crystal Growth & Design. 2007, 7 (12), 2568–2575.

[90] W.L. Suchanek, R.E. Riman, Hydrothermal synthesis of advanced ceramic powders, Advances in Science and Technology. 2006, 45, 184–193.

[91] Engineering Atoms, SEM scheme, September 2016. retrieved from https://www.eng-atoms.msm.cam.ac.uk/Images/SEMScheme/image_view_fullscreen.

[92] HyperPhysics, Bragg's Law, retrieved from https://hyperphysics.phy-astr.gsu.edu/hbase/quantum/bragg.html.

[93] S. Royer, D. Duprez, F. Can, X. Courtois, C. Batiot-Dupeyrat, S. Laassiri, H. Alamdari, Perovskites as substitutes of noble metals for heterogeneous catalysis: dream or reality, Chemical Reviews. 2014, 114, 10292-10368.

[94] M. Kubicek, A. H. Bork, J. L. M. Rupp, Perovskite oxides – a review on a versatile material class for solar-to-fuel conversion processes, Journal of Materials Chemistry A. 2017, 5, 11983-12000.

[95] H. Zhu, P. Zhang, S. Dai, Recent Advances of Lanthanum-Based Perovskite Oxides for Catalysis, ACS Catalysis. 2015, 5, 6370-6385.

[96] Y. Zheng, J. Wang, B. Yu, W. Zhang, J. Chen. J. Qiao, J. Zhang, A review of high temperature co-electrolysis of H_2O and CO_2 to produce sustainable fuels using solid oxide electrolysis cells (SOECs): advanced materials and technology, Chemical Society Reviews. 2017, 46, 1427-1463.

[97] T. Wu, B. Yu, W. Zhang, J. Chen, S. Zhao, Fabrication of a high-performance nano-structured $Ln_{1-x}Sr_xMO_{3-d}$ (Ln = La, Sm; M = Mn, Co, Fe) SOC electrode through infiltration, RSC Advances. 2016, 6, 68379-68387.

[98] M. M. Nair, S. Kaliaguine, F. Kleitz, Nanocast $LaNiO_3$ perovskites as precursors for the preparation of coke-resistant dry reforming catalysts, ACS Catalysis. 2014, 4, 3837-3846.

[99] M. M. Nair, F. Kleitz, S. Kaliaguine, Kinetics of methanol oxidation over mesoporous perovskite catalysts, Chemcatchem, 2012, 4, 387-394.

[100] M. Ezbiri, M. Takacs, B. Stolz, J. Lungthok, A. Steinfeld, R. Michalsky, Design principles of perovskites for solar-driven thermochemical splitting of CO_2, Journal of Materials Chemistry A. 2017, 5, 15105-15115.

[101] N. Tsvetkov, Q. Lu, L. Sun, E. J. Crumlin, B. Yildiz, Improved chemical and electrochemical stability of perovskite oxides with less reducible cations at the surface, Nature Materials. 2016, 15, 1010-1017.

[102] M. M. Nair, S. Abanades, Insights into the redox performance of non–stoichiometric lanthanum manganite perovskites for solar thermochemical CO_2 splitting, Chemistry Select 2016, 1, 4449-4457.

[103] F. He, F. Li, Perovskite promoted iron oxide for hybrid water-splitting and syngas generation with exceptional conversion, Energy Environmental Science. 2015, 8, 535-539.

[104] D. Neagu, G. Tsekouras, D. N. Miller, H. Menard, J. T. S. Irvine, In situ growth of nanoparticles through control of non-stoichiometry, Nature Chemistry. 2013, 5, 916- 923.

[105] A. H. McDaniel, E. C. Miller, D. Arifin, A. Ambrosini, E. N. Coker, R. O'Hayre, W. Cheuh, J. Tong, Sr- and Mn-doped $LaAlO_{3-\delta}$ for solar thermochemical H_2 and CO production, Energy Environmental Science. 2013, 6, 2424-2428.

[106] J. Vieten, B. Bulfin,F. Call, M. Lange, M. Schmucker, A. Francke, M. Roeb, C. Sattler, Perovskite oxides for application in thermochemical air separation and oxygen storage, Journal of Material Chemistry A. 2016, 4, 13652-13659.

[107] E. Konysheva, J. T. S. Irvine, Thermochemical and structural stability of A- and B-site-substituted perovskites in hydrogen-containing atmosphere, Chemistry Materials. 2009, 21, 1514–1523.

[108] J. Zhang, V. Haribal, F. Li, Perovskite nanocomposites as effective CO_2-splitting agents in a cyclic redox scheme, Science Advances. 2017, 3.

[109] S. Dai, S. Zhang, M. B. Katz, G. W. Graham, X. Pan, In situ observation of rh-catio3 catalysts during reduction and oxidation treatments by transmission electron microscopy, ACS Catalysis. 2017, 7, 1579−1582.

[110] B. Moghtaderi, Review of the Recent Chemical Looping Process Developments for Novel Energy and Fuel Applications, Energy & Fuels. 2012, 26, 15-40.

[111] C. L. Muhich, B. W. Evanko, K. C. Weston, P. Lichty, X. Liang, J. Martinek, C. B. Musgrave, A. W. Weimer, Efficient Generation of H_2 by Splitting Water with an Isothermal Redox Cycle, Science. 2013, 341, 540-542.

[112] M. Rydén, A. Lyngfelt, T. Mattisson, D. Chen, A. Holmen, E. Bjørgum, Novel oxygen-carrier materials for chemical-looping combustion and chemical-looping

reforming; $La_{1-x}Sr_xFe_yCo_{1-y}O_{3-\delta}$ perovskites and mixed-metal oxides of NiO, Fe_2O_3 and Mn_3O_4, International Journal of Greenhouse Gas Control. 2008, 2, 21-36.

[113] A. H. Bork, M. Kubicek, M. Struzik and J. L. M. Rupp, Perovskite $La_{0.6}Sr_{0.4}Cr_{1-x}Co_xO_{3-\delta}$ solid solutions for solar-thermochemical fuel production: strategies to lower the operation temperature, Journal of Materials Chemistry A. 2015, 3, 15546-15557.

[114] J. R. Scheffe, D. Weibel and A. Steinfeld, Lanthanum−Strontium−Manganese Perovskites as Redox Materials for Solar Thermochemical Splitting of H_2O and CO_2, Energy & Fuels. 2013, 27(8), 4250-4257.

[115] A. H. McDaniel, E. C. Miller, D. Arifin, A. Ambrosini, E. N. Coker, R. O'Hayre, W. C. Chueh, J. Tong, Sr- and Mn-doped $LaAlO_{3-\delta}$ for solar thermochemical H_2 and CO production, Energy Environmental Science. 2013, 6, 2424-2428.

[116] B. Bulfin, J. Vieten, D. E. Starr, A. Azarpira, C. Zachaus, M. Havecker, K. Skorupska, M. Schmucker, M. Roeb and C. Sattler, Redox chemistry of $CaMnO_3$ and $Ca_{0.8}Sr_{0.2}MnO_3$ oxygen storage perovskites, Journal of Materials Chemistry A. 2017, 5, 7912-7919.

[117] J. Vieten, B. Bulfin, F. Call, M. Lange, M. Schmucker, A. Francke, M. Roebaand C. Sattler, Perovskite oxides for application in thermochemical air separation and oxygen storage, Journal of Materials Chemistry A. 2016, 4, 16352-13659.

[118] S. Singh, D. Singh, Structural, magnetic and electrical properties of Fe-doped perovskite manganites $La_{0.8}Ca_{0.15}Na_{0.05}Mn_{1-x}FexO_3$ (x = 0, 0.05, 0.10 and 0.15), Journal of Alloys and Compounds. 2017, 702, 249-257.

[119] S. Noorman, F. Gallucci, M. Van Sint Annaland, J. A. M. Kuipers, Chemical Engineering Journal. 2011, 167, 297–307.

[120] T. Mattisson, Materials for chemical-looping with oxygen uncoupling. ISRN Chemical Engineering. 2013, 2013, 1–19.

[121] Q. Imtiaz, D. Hosseini, C. R. Müller, Review of oxygen carriers for chemical looping with oxygen uncoupling (CLOU): thermodynamics, material development, and synthesis. Energy Technology. 2013, 1, 633-647.

[122] M. Arjmand, R. F. Kooiman, M. Rydén, H. Leion, T. Mattisson, A. Lyngfelt. Sulfur tolerance of $Ca_xMn_{1-y}M_yO_{3-\delta}$ (M = Mg, Ti) perovskite-type oxygen carriers in chemical-looping with oxygen uncoupling (CLOU), Energy & Fuel. 2014, 28, 1312-1324.

[123] L. Wang, D. Li, M. Koike, S. Koso, Y. Nakagawa, Y. Xu, K. Tomishige, Catalytic performance and characterization of Ni-Fe catalysts for the steam reforming of tar from biomass pyrolysis to synthesis gas, Applied Catalysis A: General. 2011, 392, 248-255.

[124] M. H. Imanieha, M. H. Rada, A. Nadarajaha, J. González-Platasb, F. Rivera-Lópezc, I. R. Martínb, Novel perovskite ceramics for chemical looping combustion application, Journal of CO_2 Utilization. 2016, 13, 95–104.

[125] L. Liu, D.l D. Taylor, E. E. Rodrigueza, M. R. Zachariah, Influence of transition metal electronegativity on the oxygen storage capacity of perovskite oxides, Chemical Communications. 2016, 52, 10369-10372.

Appendix: GSAS cell refinement

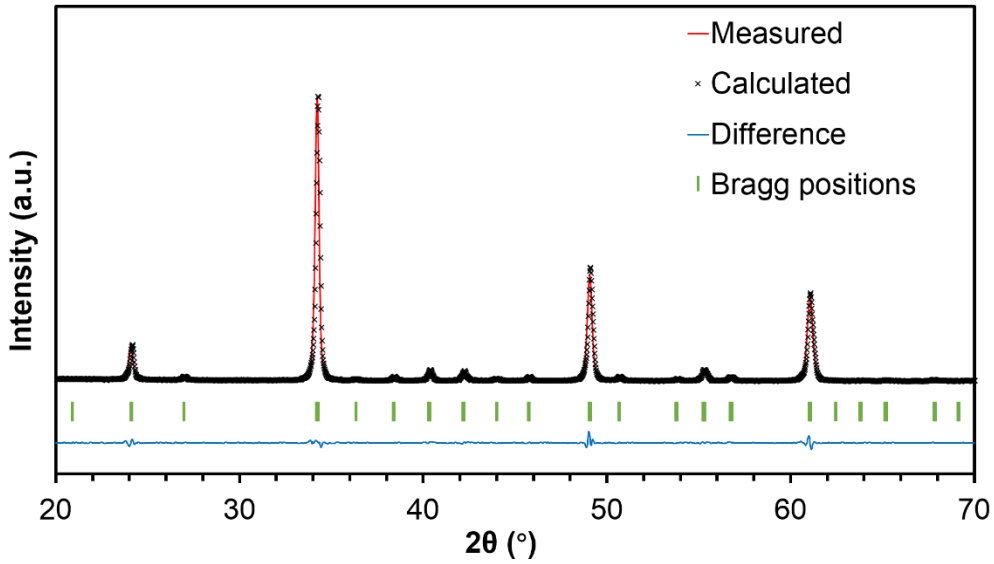

Figure A- 1. XRD data and corresponding Rietveld refinement results of CMO

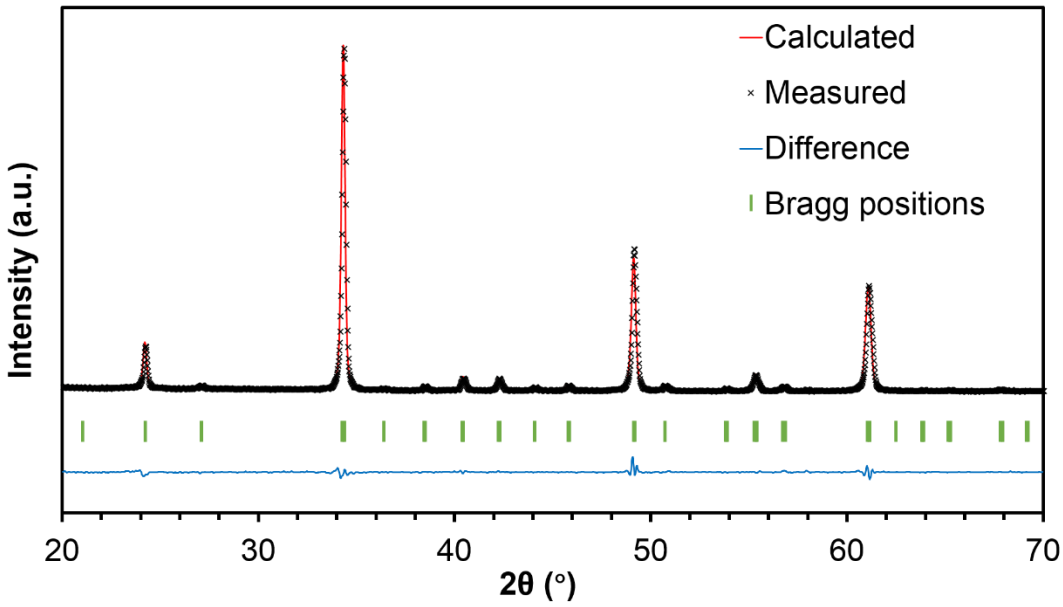

Figure A- 2. XRD data and corresponding Rietveld refinement results of CFM5P

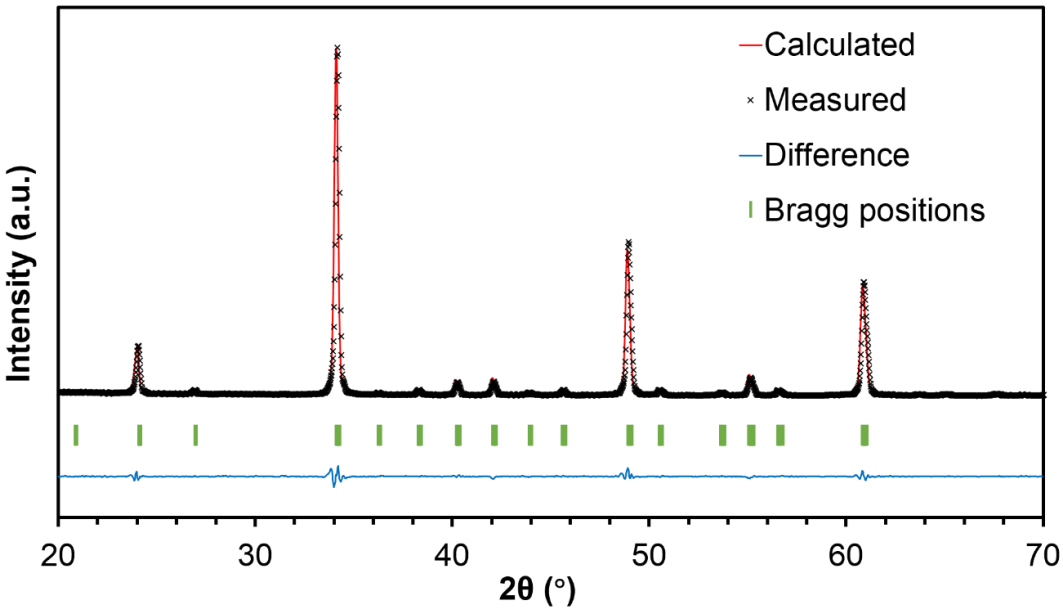

Figure A- 3. XRD data and corresponding Rietveld refinement results of CFM19

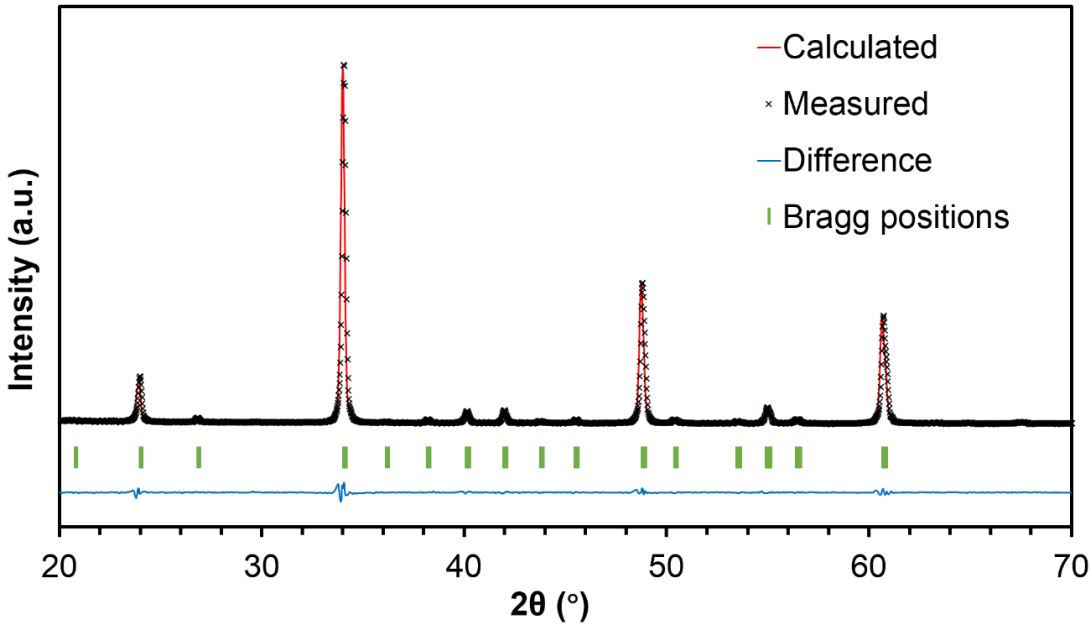

Figure A- 4. XRD data and corresponding Rietveld refinement results of CFM28